

## Unraveling the Origins of GRB X-ray Plateaus through a Study of X-ray Flares

H. DERELI-BÉGUÉ <sup>1</sup>, A. PE'ER <sup>1</sup>, D. BÉGUÉ <sup>1</sup> AND F. RYDE <sup>2</sup>

<sup>1</sup>*Department of Physics, Bar-Ilan University, Ramat-Gan 52900, Israel*

<sup>2</sup>*Department of Physics, KTH Royal Institute of Technology and The Oskar Klein Centre, SE-106 91 Stockholm, Sweden*

### ABSTRACT

The X-ray light curves of gamma-ray bursts (GRBs) display complex features, including plateaus and flares, that challenge theoretical models. Here, we study the properties of flares that are observed in the early afterglow phase (up to a few thousands of seconds). We split the sample into two groups: bursts with and without X-ray plateau. We find that the distributions of flare properties are similar in each group. Specifically, the peak time ( $t_{\text{pk}}$ ) of the flares and the ratio of the flare width to the flare peak time ( $w/t_{\text{pk}}$ ) which is found to be  $\approx 1$ , regardless of the presence of a plateau. We discuss these results in view of the different theoretical models aimed at explaining the origin of the plateau. These results are difficult to explain by viewing angle effects or late time energy injection, but do not contradict the idea that GRBs with X-ray plateau have low Lorentz factor, of the order of tens. For these GRBs, the dissipation processes that produce the flares naturally occur at smaller radii compared to GRBs with higher Lorentz factors, while the flares maintain a similar behaviour. Our results therefore provide an independent support for the idea that many GRBs have Lorentz factor of a few tens rather than a few hundreds.

*Keywords:* Gamma-ray bursts, Light Curves: X-ray, Astronomy data analysis, Relativistic jets, Radiation mechanisms: non-thermal.

### 1. INTRODUCTION

Gamma-ray bursts (GRBs) are extremely energetic events and are also known to have highly relativistic jets, with initial expansion Lorentz factors typically ranging from tens to thousands (Krolik & Pier 1991; Fenimore et al. 1993; Racusin et al. 2011; Dereli-Bégué et al. 2022). GRBs display two sequential phases: the prompt emission phase, followed by the afterglow phase. These two phases can be explained within the framework of the classical GRB fireball model (Rees & Meszaros 1992; Mészáros et al. 1998; Piran 2004; Mészáros 2006; Kumar & Zhang 2015) where the GRB prompt  $\gamma$ -ray emission is caused by internal energy dissipation (e.g., shocks) within a collimated ultrarelativistic jet, and the broadband afterglow emission is created by an external shock propagating into the circumburst medium, which can be either a stellar wind or constant density interstellar medium (ISM) (Meszaros & Rees 1997; Sari et al. 1998).

Following the launch of the Neil Gehrels *Swift* Observatory (hereafter *Swift*; Gehrels et al. (2004)), several previously unknown features in the X-ray light curves have been observed. Notably, while the late-time X-ray emission (after  $\sim 10^{3.5} - 10^4$  s), aligns with the theoretical predictions of the classical fireball model, other phenomena such as early steep decays, X-ray plateaus, and X-ray flares observed by *Swift* do not fit as straightforwardly within this model (Nousek et al. 2006; O'Brien et al. 2006; Zhang et al. 2006; Evans et al. 2007, 2009).

The early steep decay, characterized by a temporal index between  $3 \leq \alpha \leq 5$ , has been associated with the end of the prompt phase and is attributed to high-latitude emission arising from photons emitted at larger angles relative to the jet axis (corresponding to the observer direction), leading to a rapid decline in observed intensity (Barthelmy et al. 2005; Tagliaferri et al. 2005; Willingale et al. 2007; Ronchini et al. 2021). The following X-ray plateaus, with a shallow temporal index between  $0 \leq \alpha \leq 0.7$ , generally appear  $100 - 10^3$  seconds after the GRB trigger and are usually followed by a late time "afterglow" decay with an index between  $1.2 \leq \alpha \leq 1.5$  (Zhang et al. 2006; Dereli-Bégué et al. 2022), as is expected theoretically (Meszaros & Rees 1993). Therefore, the flux during the plateau phase decreases

slower than theoretically expected. This feature is observed in a substantial fraction, close to 60% of all GRBs (Evans et al. 2009; Srinivasaragavan et al. 2020).

Since its discovery in early 2005, several ideas have been proposed to explain the X-ray plateau phase. It was initially proposed that the origin of the plateau phase is a continuous energy injection into the external shock from the central compact object, which produces the energy powering the GRB. This central engine can either be a newly formed black-hole (Zhang et al. 2006; Granot & Kumar 2006; Nousek et al. 2006) or a millisecond magnetar (Metzger et al. 2011). Alternatively, it was suggested that the observed plateau is due to viewing angle effects, where structured jets are observed slightly off-axis (Eichler & Granot 2006; Toma et al. 2006; Eichler 2014; Beniamini et al. 2020a; Oganessyan et al. 2020; Beniamini et al. 2020b). Recently, we suggested a different explanation, according to which the observed signal originates from an outflow that is observed on-axis, but reaches a maximum Lorentz factor of several tens at most, expanding into a medium composed of a low density wind (Shen & Matzner 2012; Dereli-Bégué et al. 2022). It is therefore of interest to find an observational measure that could discriminate between these models.

X-ray flares typically occur  $100 - 10^5$  seconds after the prompt emission and are observed in about half of the GRB population, mostly in long GRBs but rarely in short GRBs (Burrows et al. 2005; Falcone et al. 2007; Chincarini et al. 2007; Curran et al. 2008; Chincarini et al. 2010; Margutti et al. 2011; Bernardini et al. 2011). They usually appear as one or two flares, with cases of multiple flares being rare (*e.g.* Perri et al. 2007; Abdo et al. 2011). Flares can be considerably energetic and are often characterized by large flux variations (Falcone et al. 2006; Gibson et al. 2018). Indeed, their fluence can be up to 100% of the prompt fluence, and the flare fluxes, measured with respect to the underlying continuum,  $\Delta F_{\text{flare}}/F_{\text{cont.}}$ , can vary over short timescales  $\Delta t/t_{pk} \lesssim 1$  where  $\Delta t$  measures the duration of the flare and  $t_{pk}$  is the time of maximum flare flux with respect to the trigger time (Chincarini et al. 2007). Since flares share many properties with the prompt emission, it is widely accepted that they are powered by the late central engine activities either by internal shocks (Ioka et al. 2005; Fan & Wei 2005; Zhang et al. 2006), or some other dissipation process within the ultra-relativistic outflow (Giannios 2006; Lazzati et al. 2011), but at later times and at lower energies.

Since flares are so abundant, they are observed both in GRBs with and without plateaus. Given that different theoretical models about the origin of the plateau phase have different expectations about the observed properties of flares, comparing flare properties in GRBs with and without plateaus can potentially be used as an independent way of discriminating between the different models. The only study we aware of to day is that of Yi et al. (2022), who compared the X-ray flare energy and the X-ray plateau energy with the isotropic prompt emission energy and found that all are correlated. Here, we conduct a comprehensive study on the properties of flares observed in *Swift* GRBs with and without plateaus. We then discuss the implications on the different theoretical models.

This paper is organized as follows. In Section 2, we define the data collection and analyses method with sample selection and model definition as well as fitting procedure and best model selection. In Section 3, we present the flare analysis results. In Section 4, we then discuss how our definition of flares could impact the results. In Section 5, we discuss the physical interpenetration of the results. Finally, in Section 6 we list our summary and conclusions. Throughout the paper, a flat  $\Lambda$ CDM cosmological model with cosmological parameters  $\Omega_m = 0.286$  and  $H_0 = 70$   $\text{km.s}^{-1}.\text{Mpc}^{-1}$  are used (Hinshaw et al. 2009).

## 2. DATA COLLECTION AND ANALYSIS METHOD

### 2.1. Sample Selection

We selected a statistically significant sample of 100 GRBs by anti-chronologically searching through 8 years of data from the *Swift* archive, starting December 2<sup>nd</sup> 2022. As for our first paper on this topic (Dereli-Bégué et al. 2022), the selection criteria are as follow. First, the redshift of the burst has to be measured by spectroscopy. The second criteria limits the sample to those GRBs which triggered *Swift*-BAT. Indeed, GRBs which are not observed by BAT usually lack *Swift*-XRT observations, preventing us from performing the fitting procedure described in the following sections. In fact, even GRBs initially detected by *Swift*-BAT can lack a sufficiently large number of data points, and those GRBs were removed from the sample. The required number of data points is set to be  $\geq 5$  at the beginning or end of each independent decaying feature identified in the light curve.

### 2.2. Model Definition

GRB afterglow light-curves are made of several components, namely (i) the early afterglow steep decay; (ii) the plateau (when it exist); (iii) the late time afterglow ("the self-similar decay") slope; and (iv) the post-jet break decay.

On top of these, there are (v) flares (when they exist). Combining all components lead to the so-called canonical X-ray light-curve (Nousek et al. 2006; O’Brien et al. 2006; Zhang et al. 2006). Yet each component can be observed independently of the others, creating the rich afterglow phenomena, and providing a unique challenge in fitting and interpreting the afterglow light-curves.

To investigate both flare and plateau properties, our analysis method is as follows. In our approach, we model the light curve using continuous power-law segments, that can have either one, two, three or four segments. Flares are modeled using the "Norris" function (Norris et al. 2005). They are integrally part of the models and their properties are constrained during the fit, alongside those of the underlying afterglow. For full details of the fitting procedure, see section 2.3 and Appendix A below.

The difficulty in handling multi-component models, considering for instance several flares, the underlying afterglow emission and eventually a jet break, is due to the large number of parameters and the resulting high model flexibility, which allows the "naive" model to fit any light-curve at the expense of a physical interpretation. A solution to this problem is to prescribe conditions that are simultaneously sufficiently general for the model to accurately represent the data or clearly fail when attempting to do so, while also being sufficiently physically motivated to obtain meaningful and interpretable results.

Here, we choose to fit each X-ray light curve, starting from the "steep decay" phase (when it exists). Following the steep decay, we apply a physically motivated afterglow model, based on synchrotron emission from particles accelerated by the propagating forward shock wave, assuming spherical symmetry. The shock-accelerated electrons assume a power-law distribution, with power law index  $p$ , in between Lorentz factors  $\gamma_{\min}$  and  $\gamma_{\max}$ . This leads to two relevant characteristic frequencies in the observed spectra,  $\nu_m$  which is the typical emission frequency from electrons at  $\gamma_{\min}$ , and  $\nu_c$  which is the cooling frequency. As was shown by several authors (e.g. Granot & Sari 2002; Dereli-Bégué et al. 2022), various combinations of light curves and spectra can be obtained. The resulting light curve depends on (i) the evolutionary stage of the blast wave propagation - coasting vs. self similar decaying phase; (ii) the ambient medium profile- stellar wind or constant density ISM; and (iii) the observed frequency, which can be smaller, larger or in between  $\nu_m$  and  $\nu_c$ .

In addition to the above mentioned possibilities, when fitting the light curves, we add three additional categories: (i) A steep decay is fitted as a power law in time, with a slope that is independent on the electrons power law index and steeper than 2; (ii) inclusion of a jet break; and (iii) number of flares, which we consider to vary in between 0, 1 or 2. Combined together, we consider a total of 36 different models used in fitting the data. Although the models we use assume spherical symmetry, we point out that deviation from spherical symmetry predictions are expected at late times (after the jet break), while all the flares identified occur at much earlier times, before the jet break. Therefore, the key properties of the flares we are interested in (peak time and flare width) are only weakly sensitive to this assumption. For a complete description of the models used, see Appendix A.

In our analysis, flares take the shape of a Norris function (Norris et al. 2005; Chincarini et al. 2010),

$$\mathcal{N}(T) = A_f \lambda \exp \left[ -\frac{\tau_1}{T - t_0} - \frac{T - t_0}{\tau_2} \right], \quad (1)$$

if  $T > t_0$  and  $\mathcal{N}(T) = 0$  otherwise. Here,  $A_f$  is the flare amplitude,  $t_0$  is the onset time of the flare,  $\tau_1$  and  $\tau_2$  are two flare shape parameters related to the rise and decay phases altering the flare profile and in particular its asymmetry, and  $\lambda = \exp(2\mu)$  where  $\mu = (\tau_1/\tau_2)^{1/2}$ . The maximum of the flare is reached at time  $t_{\text{pk}} = t_0 + (\tau_1\tau_2)^{1/2}$  and its maximum equals to  $\mathcal{N}(t_{\text{pk}}) = A_f$ . The factor  $A_f$  quantifies the relative enhancement of the flux due to the flare. Following Chincarini et al. (2010) and noting that we fit the logarithm of the flux, one can define the flare flux variability,

$$\frac{\Delta F_{\text{flare}}}{F_{\text{cont.}}} = \frac{10^{\mathcal{N}(t_{\text{pk}})} 10^{F_{\text{cont.}}} - 10^{F_{\text{cont.}}}}{10^{F_{\text{cont.}}}} = 10^{\mathcal{N}(t_{\text{pk}})} - 1. \quad (2)$$

where  $F_{\text{flare}}$  and  $F_{\text{cont.}}$  are the flare and underlying afterglow fluxes.

An important property of X-ray flares is their temporal aspect ratio  $w/t_{\text{pk}}$ , where  $w$  is the flare temporal width. Flare width has been estimated in various ways and using different functions, including e.g. a symmetric Gaussian (Chincarini et al. 2007), a smoothly broken power-law profile (Yi et al. 2016), and using the Norris function (Norris et al. 2005). For the latter, Chincarini et al. (2010); Bernardini et al. (2011) define the flare width  $w$  as the time interval during which the contribution of the flare is larger than  $1/e$  of its maximum, leading to  $w = \Delta t_{1/e} = \tau_2(1 + 4\mu)^{1/2}$ . We cannot use this definition directly, since the fits are performed in log-space. Instead, we determine the times  $\bar{t}_1$

and  $\bar{t}_2 > \bar{t}_1^1$ , between which the Norris function has value at least half of its maximum. The width is then define as

$$w = 10^{\bar{t}_2} - 10^{\bar{t}_1}, \quad (3)$$

Furthermore, it is important to note that different definitions of flare widths can lead to variations in absolute width measurements. For instance, the Full Width at Half Maximum (FWHM) may provide a narrower estimate compared to widths calculated at lower thresholds, such as 5% of the maximum flux. However, the overall characterization of  $w/t_{\text{pk}}$  remains consistent across these definitions. Defining  $w$  at 5% of the maximum captures a broader interval around the peak than the FWHM, while still providing a similar interpretation in temporal analyses, particularly when comparing the relative timescales of flares.

Moreover, while the choice of model — such as the asymmetric Norris profile (Norris et al. 2005) — may produce different width measurements compared to symmetric Gaussian profiles (Chincarini et al. 2007), these alternative definitions do not substantially affect the theoretical interpretations of physical processes. Thus, although definitions differ, the temporal ratio  $w/t_{\text{pk}}$  provides a robust measure across various models, allowing for a consistent interpretation of flare variability and duration.

The isotropic-equivalent energy  $E_{\text{iso},f}$  emitted in each flare can be calculated once the fit is performed. We calculate it using

$$E_{\text{iso},f} = 4\pi d_L^2 \cdot C_F \cdot \int_{\bar{t}_1}^{\bar{t}_2} 10^{F_{\text{cont.}}} \left(10^{N(T)} - 1\right) 10^T \ln(10) dT. \quad (4)$$

Here,  $d_L$  is the luminosity distance and  $C_F$  is the flux conversion factor, which converts count rate to flux (obtained from the online *Swift* repository). The integral represents the total count rate of the flare between  $\bar{t}_1$  and  $\bar{t}_2$ . We point out that the total energy is not sensitive to the exact choice of the integration boundaries, as the flux rises and decays exponentially.

Finally, for comparison with previous studies (e.g. Norris et al. 2005; Chincarini et al. 2010), we define the flare asymmetry,

$$k = (1 + 4\mu)^{-1/2}. \quad (5)$$

### 2.3. Fitting procedure

The X-ray count rate light curves (hereinafter LCs) of each GRB have been downloaded from the online *Swift* repository<sup>2</sup> (Evans et al. 2007, 2009), considering the full *Swift*-XRT bandpass, *i.e.*  $(E_{\text{min}}, E_{\text{max}}) = (0.3, 10)$  keV. We then fit each individual LCs to all 36 considered models, all described in section 2.2 and Appendix A. Although the light curves could have been sorted into categories in order to reduce the number of models per light-curve, we decided against this to avoid introducing human bias into the analysis process and best model selection.

To perform the fit, we assume a Gaussian likelihood and sample the posterior distributions with MultiNest (Feroz et al. 2009), a nested sampling algorithm designed for efficient Bayesian inference. We assume 8000 (1000 for the model without flares) active points and a tolerance of 0.5 to ensure efficient sampling and convergence. MultiNest offers a number of advantages, including computational efficiency and the ability to robustly handle multi-modal posterior distributions, which is a relevant possibility given the high dimensionality and complexity of the parameter space for the models we considered, specifically for those with one or two flares. Multinest also computes the evidence, which is the key to perform model comparison, see section 2.4.

The parameter ranges and their sampling distributions, either uniform or log-uniform, are summarized in Table 1. For example, the electron power-law index  $p$  is sampled linearly from a non-informative uniform prior within the range of 2 to 3, similar to the parameters  $A$ ,  $b$ ,  $q$ ,  $A_{f1}$ ,  $A_{f2}$  as seen in Table 1. Parameters related to time *i.e.*,  $T_1$ ,  $T_2$ ,  $T_3$  as well as the rise and decay time parameter for the Norris function for the flares follow log-uniform priors to account for their wide range and scale sensitivity.

In our analysis, for the flare amplitude, we set a minimum value of 0.2 for  $A_{f1}$ ,  $A_{f2}$ , corresponding to an increase by a factor of 1.58 for the flare flux relative to the underlying continuum in the linear scale. This ensures that the flare flux is always at least 1.58 times larger than the underlying continuum flux, allowing for clear identification of flares and preventing the misidentification of small random flux variations in the light curve as flares.

<sup>1</sup> We note these times  $\bar{t}$  to avoid confusion with the break time of the afterglow  $T_1$ ,  $T_2$  and  $T_3$

<sup>2</sup> [https://www.swift.ac.uk/xrt\\_curves/](https://www.swift.ac.uk/xrt_curves/)

Parameter	Units	Minimum	Maximum	Type of distribution
$T_1$	s	xdata(min)	4	Logarithmic
$T_2$	s	0.5	3	Logarithmic
$T_3$	s	0.5	3	Logarithmic
$A$	-	-10	10	Linear
$b$	-	-5	-2	Linear
$p$	-	2	3	Linear
$q$	-	0	1.5	Linear
$t_1$	s	xdata(min)-0.1	3.5	Logarithmic
$A_{f1}$	-	0.2	3	Linear
$\tau_{1,1}$	s	-2.1	-0.2	Logarithmic
$\tau_{1,2}$	s	-2.1	-0.2	Logarithmic
$t_2$	s	0.2	2	Logarithmic
$A_{f2}$	-	0.2	3	Linear
$\tau_{2,1}$	s	-2.1	-0.2	Logarithmic
$\tau_{2,2}$	s	-2.1	-0.2	Logarithmic

**Table 1.** Parameters used in the fitting procedure. For each parameter we include its units, prior allowed ranges and the sampling distribution. The parameters are divided into two parts. The top part includes the parameters of the underlying afterglow:  $T_1$ ,  $T_2$ , and  $T_3$  represent the break times;  $A$  is the normalization;  $b$  is the slope of the steep decay;  $p$  is the electron power-law index; and  $q$ , together with  $p$ , defines the slope of the decay phase after the jet break (see Appendix A). The bottom part includes the parameters of the flares when present:  $t_1$  and  $t_2$  are the start times of the flares;  $A_{f1}$  and  $A_{f2}$  are the flare amplitudes; and  $\tau_{1,1}$ ,  $\tau_{1,2}$ ,  $\tau_{2,1}$ , and  $\tau_{2,2}$  are the rise and decay time parameters that shape the flare profiles.

#### 2.4. Best model selection and verification

Our best model selection is based on the Bayesian model comparison methods and the following strategy. The first step is to discard cases where there is a lack of data near the peak time of the flare. One of the challenges in analyzing GRB X-ray data is the lack of observations, specifically on the time scale of a few thousands seconds, corresponding to the orbit time of Swift (*e.g.*, Earth occultation), which can significantly affect the accuracy of the model fitting. To address this, we incorporate a criterion that considers the density of data points around the peak time of each flare. Specifically, if there are fewer than two data points within the time interval from the start to the peak of the flare, the model is flagged as unreliable and the model is discarded from further consideration. Indeed, this situation arises when a single or two data points within the full LC can be better explained by a very narrow flare. In fact, this criterion ensures that the model has sufficient data to accurately characterize the rise, the peak and the decay of the flare.

In the next step, we aim to balance the complexity of the model with its ability to fit the data well. This is achieved by prioritizing models with fewer parameters, provided they adequately capture the observed phenomena. The potential best models are identified for each case (C/F and E for the wind or H and G for the ISM, see Appendix A for details on the nomenclature) by comparing nested models one by one based on the Bayes factors and excluding those with a Bayes factor larger than 5. This process ensures that only models with balanced performance and fewer parameters are advanced to the next stage. While this initial selection narrows down the models effectively, Bayes factors are not always well-suited for non-nested model comparisons, as prior choices can be heavily influence the Bayes factor. To address this limitation, we adopt AIC as an additional criterion. AIC and AICc (corrected Akaike Information Criterion) provide a consistent framework for comparing non-nested models. Therefore, among all potential models, the best model is selected based on the lowest AICc value, as AICc accounts for potential over-fitting and bias, particularly in models with small sample sizes. If AICc is unavailable, the model with the lowest AIC is chosen instead. Finally, the residuals between the model and the data are computed for each selected model and visually inspected to ensure that it does not exhibit outliers — namely data points with residuals significantly different from the others — or systematic deviations, which are consistent patterns of misfit. Once the fit are finished and the analysis performed, we exclude 11 GRBs from the remaining of the analysis, as in these GRBs flares were misidentified, resulting in failures of the different afterglow models to adequately fit the data. A detailed description of the reasoning for excluding these eleven GRBs are provided in Appendix B.

### 3. FLARE ANALYSIS RESULTS

From the remaining 89 bursts in our sample, we find the following.

- (i) 61 bursts (69% of GRBs in our sample) have flares. This indicates that flares are quite common in GRB afterglows. This value is slightly higher than previously reported, where about half of the GRBs were found to exhibit flares (Zhang et al. 2006; Chincarini et al. 2010).
- (ii) 57 GRBs in our sample (64%) have an X-ray plateau.
- (iii) Among the 61 GRBs with flares, 42 (68%) have a plateau, while 19 bursts do not.
- (iv) Of the 57 GRBs that have a plateau, 42 (73%) also exhibit flares.

These results imply that the overall occurrence of flares in GRBs without a plateau phase ( $19/32 = 59\%$ ) does not statistically differ from the occurrence of flares in GRBs with a plateau phase ( $42/57 = 73\%$ ). This strongly suggests that the presence of flares is independent of the existence of a plateau, indicating that these two phenomena, namely plateaus and flares are most likely not related or dependent on each other.

Here, we focus on analyzing the properties of flares, and we therefore focus on the sub-sample of 61 GRBs with flares. A complete analysis of the afterglow properties of all GRBs in our sample will appear elsewhere (Dereli-Bégué et al., in prep.). The properties of all flares that appear in the 61 bursts in our sample are listed in Table C1 in Appendix C.

#### 3.1. Flare energetic, time of occurrence and duration

In order to study possible correlations between flare properties and existence of a plateau, we split the flare sample into two. The first part contains 65 flares identified in the X-ray LCs of 42 bursts with a plateau phase, while the second part includes 32 flares identified in the LCs of 19 GRBs without a plateau phase. Figure 1 shows the distributions of the flare peak times  $t_{\text{pk}}$ , the flare width  $w$ , and the flare isotropic energy  $E_{\text{iso},f}$ . Flares that originate from bursts with plateau are colored in purple, and those that are detected in GRBs without plateau are in red. Comparing the averages, we find that  $\langle \log_{10} t_{\text{pk}} \rangle = 2.64 \pm 0.08$  for GRBs with a plateau, to be compared with  $\langle \log_{10} t_{\text{pk}} \rangle = 2.79 \pm 0.11$  for burst without a plateau. A similar result holds for the width  $w$  and the flare isotropic energy  $E_{\text{iso},f}$ , with  $\langle \log_{10} w \rangle = 2.89 \pm 0.11$  and  $\langle \log_{10} E_{\text{iso},f} \rangle = 51.43 \pm 0.12$  to be compared to  $\langle \log_{10} w \rangle = 3.02 \pm 0.16$  and  $\langle \log_{10} E_{\text{iso},f} \rangle = 51.49 \pm 0.17$  for bursts with and without plateau, respectively. We further performed a Kolmogorov-Smirnov (KS) test for each parameter and find that (i) KS test statistic is  $D = 0.23$  with a probability  $p = 0.18$  for  $t_{\text{pk}}$ ; (ii)  $D = 0.11$  and  $p = 0.92$  for the width; and (iii)  $D = 0.10$  and  $p = 0.96$  for  $E_{\text{iso},f}$ . These results show that the two sub-samples originate from the same population. We therefore conclude that the flares origin and properties are independent on the afterglow properties, which are determined by the ambient medium and forward shock properties. In particular, this means that flares are independent of the existence of a plateau phase. This conclusion is aligned with the conclusion of Chincarini et al. (2010), who similarly argued that flare properties are independent of the ambient medium (though plateaus were not considered in that work).

Furthermore, from Figure 1, we find that both sub-samples show a heavy tail toward high flare peak times and widths. This may indicate a possible existence of two populations of flares, namely narrow and wide flares. We point out that the current statistics in this region of the parameter space is small. An analysis of the complete sample of bursts observed with *Swift* would allow to resolve this issue and firmly confirmed the existence of two kinds of flares.

In Figure 2, we present the distribution of the ratio of the flare width to the flare peak time  $w/t_{\text{pk}}$  and the distribution of the flare flux variability  $\Delta F_{\text{flare}}/F_{\text{cont.}}$ . Comparing the averages, we find that  $\langle \log_{10} w/t_{\text{pk}} \rangle = 0.25 \pm 0.07$  for GRBs with a plateau, to be compared with  $\langle \log_{10} w/t_{\text{pk}} \rangle = 0.22 \pm 0.09$  for burst without a plateau. A similar result holds for the flux variability,  $\langle \log_{10} \Delta F_{\text{flare}}/F_{\text{cont.}} \rangle = 0.63 \pm 0.07$  to be compared with  $\langle \log_{10} \Delta F_{\text{flare}}/F_{\text{cont.}} \rangle = 0.63 \pm 0.11$  for bursts with and without a plateau, respectively. A KS test for each parameter reveals  $D = 0.12$  and  $p = 0.88$  for  $w/t_{\text{pk}}$ , and  $D = 0.08$  and  $p = 0.99$  for  $\Delta F_{\text{flare}}/F_{\text{cont.}}$ . These results again show that the two sub-samples originate from the same population. An important result is that the ratio of the flare width to the flare peak time ( $w/t_{\text{pk}}$ ) is approximately 1, regardless of the presence of a plateau.

**Additional checks.** In the analysis presented in this section, we considered all flares obtained from both the window timing (WT) mode and the photon counting (PC) mode of the *Swift*-XRT instrument, irrespective of the burst duration  $T_{90}$ . Therefore, the sample of flares might be contaminated by episodes of the prompt emission, namely the flares identified at early times in our analysis might be due to late prompt phase activity. To understand if these

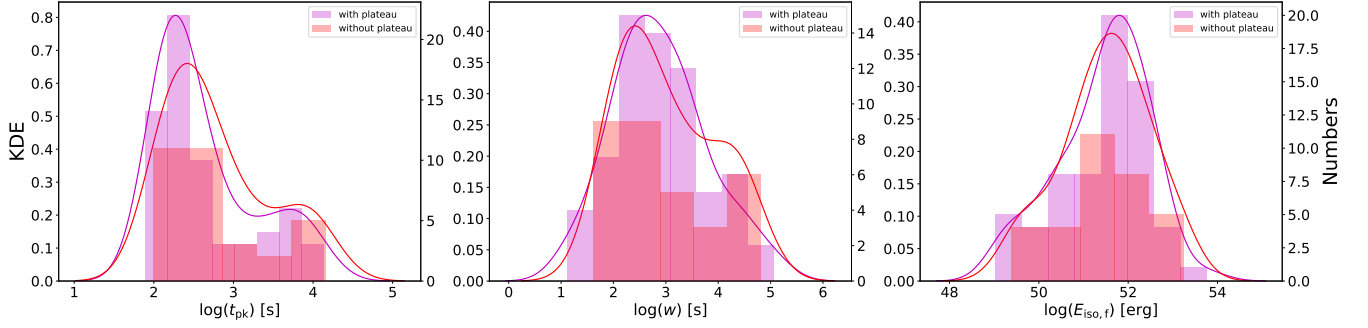


**Figure 1.** Distributions of the flare peak time,  $t_{pk}$  (left), the flare width  $w$  (middle), and the flare isotropic energy,  $E_{iso,f}^{\dagger}$  (right). The 65 flares obtained from the 42 bursts with a plateau phase are in purple, while the 32 flares obtained from the 19 GRBs without a plateau phase are in red. In each panel, the right-hand ordinate shows the number of bursts in each bin while the left-hand ordinate shows the value of the kernel density estimation (KDE) drawn by the purple and red solid lines. These distributions show that the properties of the flare are independent of the presence of a plateau phase in the GRBs X-ray light curves.

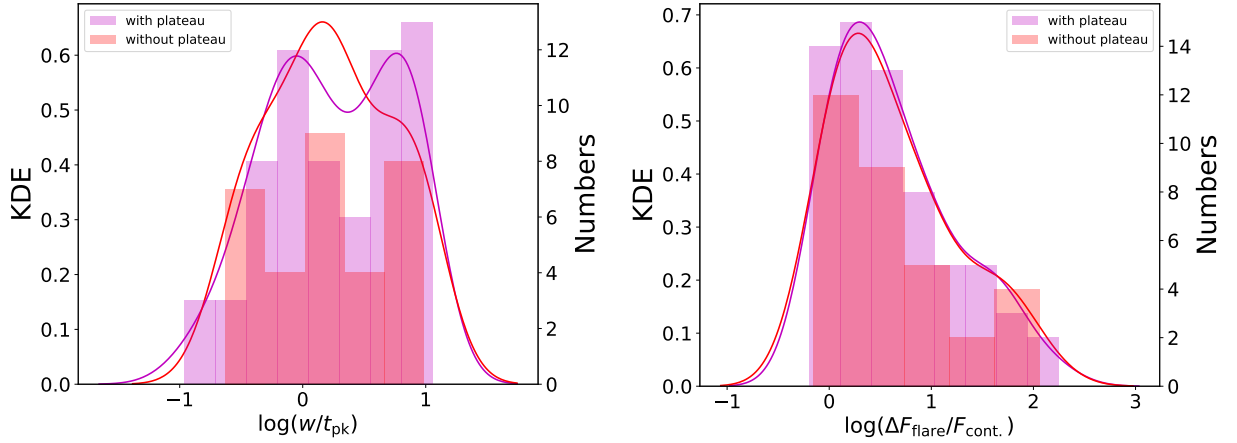


**Figure 2.** Distributions of the ratio of the flare width to the flare peak time,  $w/t_{pk}$  (left), and the flare flux variability,  $\Delta F_{flare}/F_{cont.}$  (right). The data presentation, including the color coding, is the same as in Figure 1, where purple represents the 65 flares from 42 bursts with a plateau phase, and red represents the 32 flares from 19 GRBs without plateau phases. The errors correspond to a significance of one sigma. The results show that the flare time and flux variability properties are the same, regardless of whether there is a plateau phase in the GRBs X-ray light curves. Additionally, bimodal distributions are observed in both sub-samples in the distributions of the ratio of the flare width to the flare peak time. This bi-modality is more pronounced for the GRBs with a plateau phase.

flares impact the results, we applied an additional criteria to the flare sample, considering only the flares characterized by  $t_{pk} > T_{90}$ , and repeated the analysis. This cut resulted in the exclusion of 11 flares for bursts with a plateau phase and 4 flares for bursts without a plateau phase. We found that the conclusions remain unchanged after applying this additional cut. In particular, we find that  $\langle \log_{10} t_{pk} \rangle = 2.73 \pm 0.09$  for GRBs with a plateau, compared with  $\langle \log_{10} t_{pk} \rangle = 2.86 \pm 0.12$  for bursts without a plateau.

In addition, it has been suggested that there may be a distinction between early ( $t_{pk} < 1000$  s, as studied, e.g. by Chincarini et al. 2010; Duque et al. 2022) and late flares ( $t_{pk} \geq 1000$  s, e.g. Bernardini et al. 2011). Considering this possibility as well, we limited the sample to flares for which  $T_{90} < t_{pk} < 1000$  s, ensuring that the flares are not contaminated by the prompt emission and occur at early times. As a result of this additional criteria, the sample size was significantly reduced, comprising 38 flares for GRBs with a plateau phase and 18 flares for GRBs without a plateau phase. Despite this stringent selection criteria and substantially reduced-sized sample, the ratio  $w/t_{pk}$  remains the same, enlightening the solidity of this result.

### 3.2. Correlations between flare parameters

The relation between the peak time  $t_{\text{pk}}$  and the width  $w$  of each X-ray flare is presented in Figure 3. The result of the Spearman’s rank correlation coefficient  $r = 0.68$  (0.77) with a corresponding chance probability of  $p \ll 10^{-2}$  ( $\ll 10^{-2}$ ) shows a strong positive correlation between the width  $w$  and the  $t_{\text{pk}}$  for both sub-samples with and without plateau respectively. This indicates that the longer the peak time  $t_{\text{pk}}$ , the wider the flare. We performed a fit to the correlation using the functional form  $t_{\text{pk}} = C \cdot w^r$ , where  $C$  is the proportionality constant and  $r$  is a power-law index. To account for uncertainties, large errors in the data were capped at the median uncertainty value, reducing the impact of highly uncertain points. We found the power-law index  $r = 0.87 \pm 4.2 \times 10^{-5}$  for burst with plateau and  $r = 0.97 \pm 5.9 \times 10^{-5}$  for bursts without a plateau.

This result is in agreement with the previous findings of Chincarini et al. (2007, 2010); Bernardini et al. (2011); Yi et al. (2016), albeit in our analysis, we find that this correlation remains true for GRBs with and without a plateau, underlying once more that flares do not seem to be associated to the phenomena giving rise to the plateau. We note that Chincarini et al. (2007) and Chincarini et al. (2010) interpreted this tight correlation between  $t_{\text{pk}}$  and width  $w$  as an indication that flares are somewhat different from prompt phase episodes, as they do not follow such a correlation.

One of the characterizing properties of a flare temporal behavior is its asymmetry. There are two ways of displaying the flare asymmetry, either by studying  $k$  given in Equation 5 or by analyzing the relation between  $t_{\text{rise}}$  and  $t_{\text{decay}}$ . In this work, we focus on the first option. In Figure 4, we find that the means of  $k$  are 0.46 and 0.43 for both the sub-samples with a standard deviation of 0.02. These values are consistent with those found in Norris et al. (2005); Chincarini et al. (2010), where the median values are 0.49 and 0.35 with standard deviations of 0.26 and 0.2 for flares and prompt pulses, respectively.

## 4. DISCUSSION: HOW TO DEFINE A FLARE ?

In our analysis, to identify a flare over the underlying continuum, we defined a minimum flare amplitude of 0.2 (corresponding to a factor 1.58 in linear scale), which results in a flux cut. This is clearly visible in the flare-flux variability distribution,  $\Delta F_{\text{flare}}/F_{\text{cont.}}$ , shown in Figure 2 (right). This approach naturally integrates the criteria for significant flare detection into the fitting process without the need for additional checks, providing a robust criterion for distinguishing significant flares from minor variations in the afterglow. While there is no universally accepted threshold in the literature, similar empirical criteria have been used in previous studies to identify significant flares. For instance, Chincarini et al. (2010) employed a combination of visual inspection and statistical analysis to identify flares in X-ray light curves, emphasizing the importance of clear deviations from the afterglow model. Similarly, Margutti et al. (2011) utilized timing, duration, and flux increase criteria without specifying a strict numerical threshold, instead focusing on the statistical significance of the observed deviations. Our chosen threshold is consistent with these approaches, providing a balance between sensitivity to genuine flares and robustness against stochastic variations. By ensuring that detected flares exhibit a substantial increase in flux, our method aligns with the practices of Falcone et al. (2007), who required statistically significant increases in flux over the underlying afterglow. This threshold, therefore, offers a practical and validated approach to identifying significant flares in the context of our data and analysis framework.

Furthermore, in our analysis, we fit the data on a logarithmic scale, as opposed to the linear scale used in previous works. This approach provides several advantages. For instance, we identify one or two smoother flares in each light curve, compared to previous studies that reported between one and seven or even more flares (Falcone et al. 2007; Chincarini et al. 2010). The resulting widths of the flares, as shown in Figure 1 (middle), appear broader than those previously reported by Chincarini et al. (2010), such as in GRB 051117A (see Fig. 1 therein). Additionally, in Figure 2 (right), the flux variation  $\Delta F_{\text{flare}}/F_{\text{cont.}}$  peaks at approximately 5 irrespective of the environment, with a tail extending beyond 100. This result is consistent with the findings of Chincarini et al. (2010) (see their Fig. 13) and Margutti et al. (2011) (see their Fig. 7). The only difference is that the tail is shorter, not extending to 1000, and the second population is less clearly visible than in Margutti et al. (2011). This discrepancy might be due to our use of the logarithmic scaling.

Moreover, we calculate the ratio of the flare width to the flare peak time  $w/t_{\text{pk}}$  based on fits using an asymmetric model (Norris et al. 2005), following the approach of Chincarini et al. (2010). In this model, the width  $w$  is defined as the distance between two points where the function has dropped to 37% (or  $1/e$ ) of its peak value. We find that the ratios of  $w/t_{\text{pk}}$  are approximately  $0.25 \pm 0.07$  (1.78 linear scale) and  $0.22 \pm 0.09$  (1.66 linear scale) for GRBs with and without a plateau, respectively (see section 3.1). We find that our values are significantly larger than the  $0.23 \pm 0.14$  reported by Chincarini et al. (2010), which was comparable to the  $0.13 \pm 0.10$  result in Chincarini et al. (2007), where



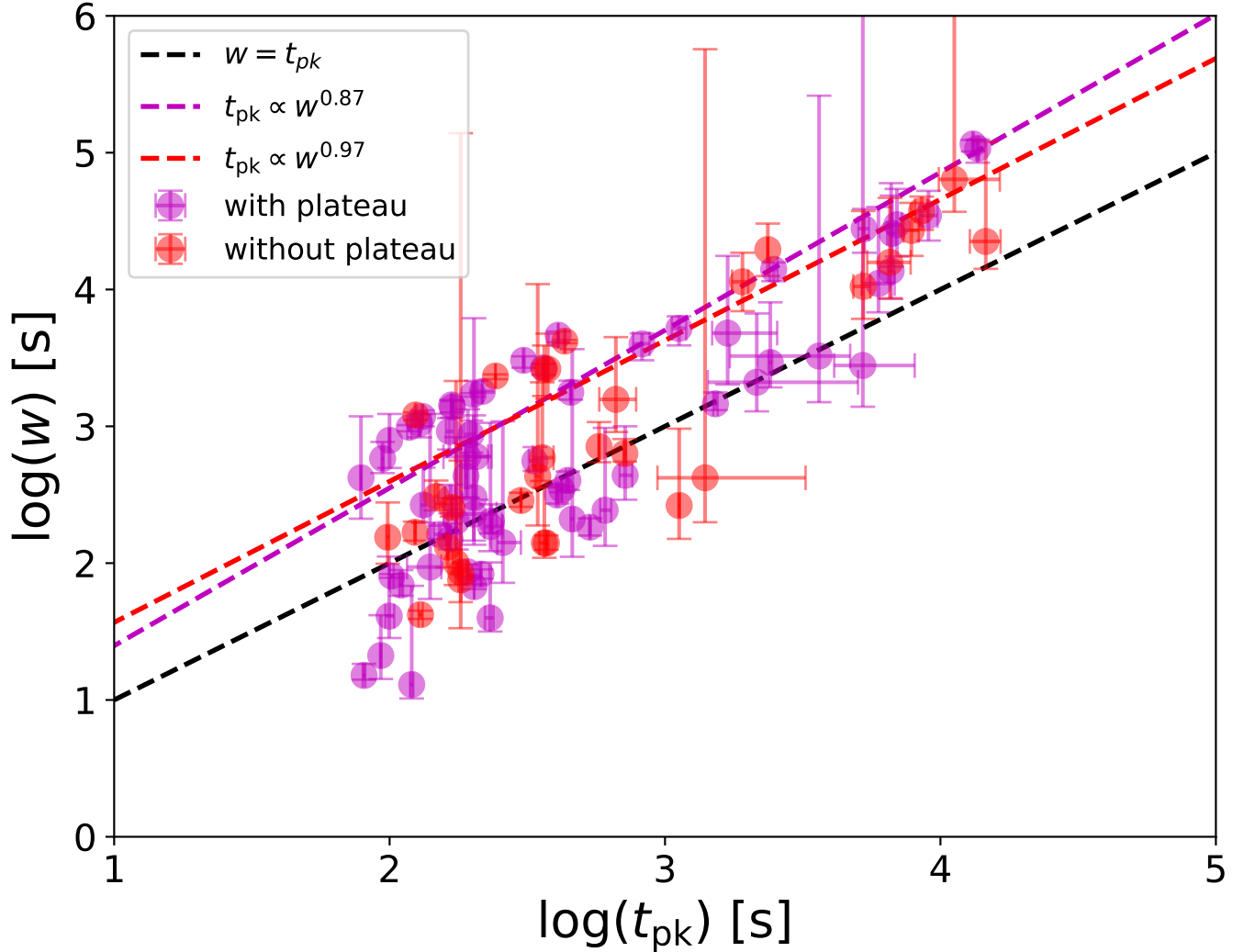


**Figure 3.** The relation between flare peak time ( $t_{pk}$ ) and flare width ( $w$ ). The purple points represent the 42 GRBs (65 flares) with plateau phases, while the red points represent the 19 GRBs (32 flares) without plateau phases in our sub-samples. The Spearman’s rank correlation coefficient  $r = 0.68$  (0.77), corresponding to a chance probability of  $p \ll 10^{-2}$  ( $\ll 10^{-2}$ ) indicates a strong monotonic relationship for GRBs with plateau phase (without plateau phase). To model the power-law relationship between  $t_{pk}$  and  $w$ , we performed a fit and find the power-law index to be  $r = 0.87 \pm 4.2 \times 10^{-5}$  and  $r = 0.97 \pm 5.9 \times 10^{-5}$  for GRBs with and without a plateau phases respectively. The fitted relations are shown as dashed purple and red lines, respectively, matching the color coding of the data points. Additionally, the line of  $w = t_{pk}$  is overlaid.

a narrower Gaussian fit was used under the assumption of symmetric flares<sup>3</sup>. After converting to the Gaussian width at 37%, they found the width to be 2.83 times the Gaussian standard deviation (resulting in  $w/t_{pk} = 0.28$ ). However, this is still lower than the values we obtain in our analysis.

In contrast, our result is consistent with what [Lazzati & Perna \(2007\)](#) found. In their analysis, by assuming a spectral index  $\beta \simeq 1$  they found  $w/t_{pk} \sim 0.83$ . This value aligns more closely with our findings of approximately 1.78 and 1.66 for GRBs with and without a plateau, respectively, although it still contrasts with the lower value of  $0.23 \pm 0.14$  reported by [Chincarini et al. \(2010\)](#).

## 5. PHYSICAL INTERPRETATION

<sup>3</sup> In their analysis, the ratio of the flare width to the flare peak time was defined as  $\Delta_t/t$  where  $\Delta_t$  is the Gaussian width defined by  $f = 0.05$ , which refers to a specific point in time where the flux of a flare has decreased to 5% of its maximum value, and  $t$  is the Gaussian peak ([Chincarini et al. 2007](#)).

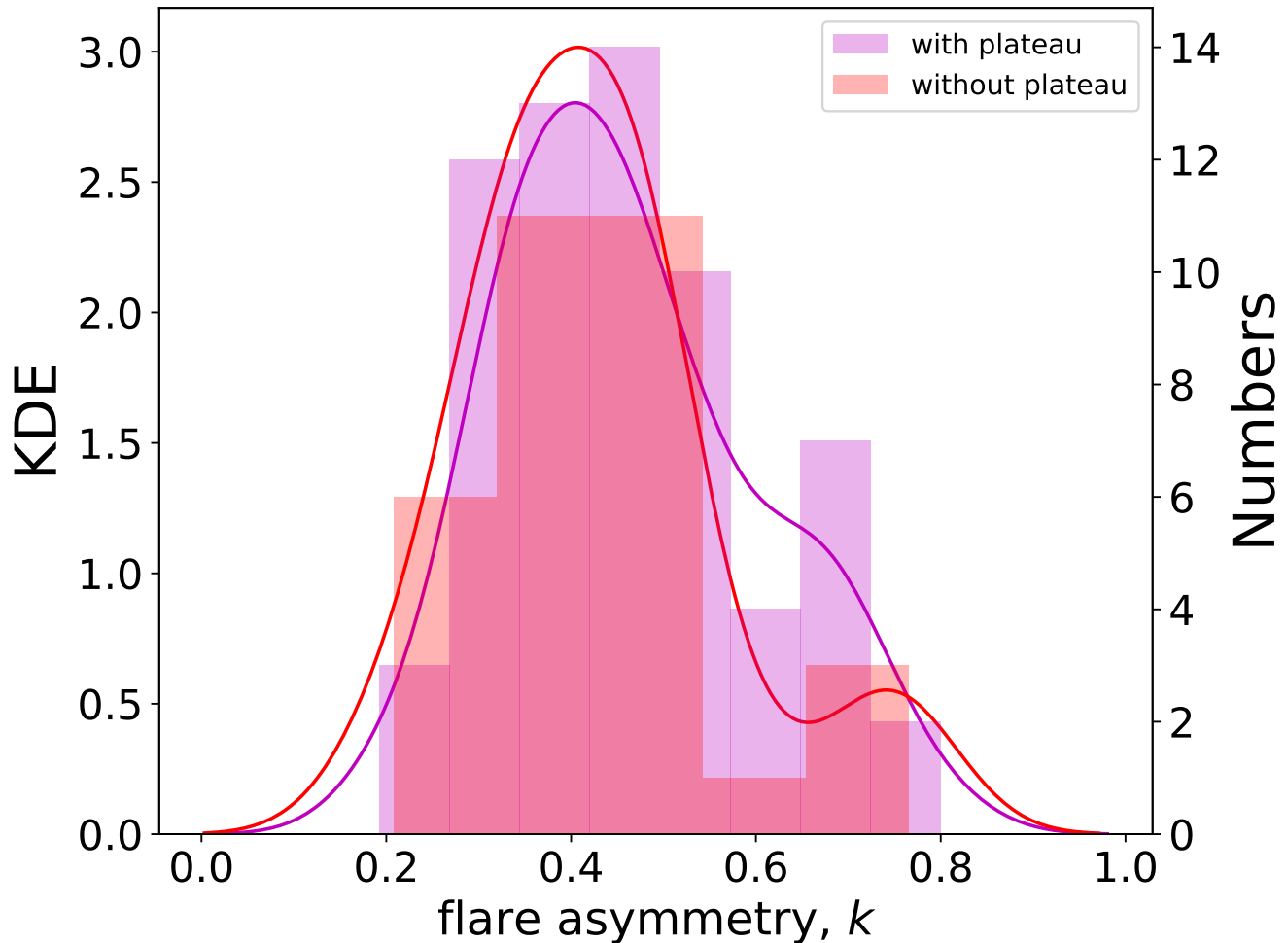


**Figure 4.** Distributions of the flare asymmetry,  $k$ . The purple bars represent the 42 GRBs (65 flares) with plateau phases, while the red bars represent the 19 GRBs (32 flares) without plateau phases. In each panel, the right-hand ordinate shows the number of burst in each histogram bin and the left-hand ordinate shows the value of the KDE, which is represented by the purple and red curves for each sample respectively. We also performed Kolmogorov-Smirnov test for the flare asymmetry,  $k$  (KS test:  $D = 0.21$  and  $p = 0.23$ ).

By studying GRBs with flares and separating them into two sub-samples, namely with or without a plateau phase, we found that the properties of the flares are independent of the existence of a plateau phase. This fact offers critical insights into the proposed emission models underlying the plateau phase.

The two key results we find are:

- (1) The flare peak time,  $t_{pk}$ , as seen in the Figure 1 (left), is on average the same for both sub-samples, with and without plateau phases.
- (2) Similarly, the ratio of the flare width to the flare peak time, as shown in Figure 2 (left), is approximately unity, irrespective of the existence of plateau. As discussed in section 3.1, removing possible prompt contamination or considering only early flares, do not change these results.

X-ray plateaus are ubiquitous in GRB's X-ray light curves. Approximately 60% of GRBs exhibit this phase (Evans et al. 2009; Srinivasaragavan et al. 2020). This slower than theoretically expected decline in flux in the early X-ray light curve challenged theoretical modeling for two decades now. Over the years, several models were suggested to explain this phenomenon. Here, we highlight some of the most discussed ones, and confront their predictions with the obtained results.

The first model suggested in the literature considers late-time continuous energy injection (Zhang et al. 2006; Nousek et al. 2006; Granot et al. 2006). This model explains the plateau phase by suggesting that late time central engine activity provides energy that is injected into the decelerating external shock. This additional energy slows down the deceleration of the shock, hence the decay of the light curve. The plateau ends when this energy injection ceases (Zhang et al. 2006; Granot et al. 2006; Granot & Kumar 2006; Fan & Piran 2006; Metzger et al. 2011). This model successfully predicts achromatic breaks across X-ray and optical bands for certain bursts, such as GRB 060729 (Grupe et al. 2007). However, it struggles to account for chromatic afterglows, where X-ray and optical light curves do not show simultaneous breaks (Nousek et al. 2006). Extensions of this model, such as the introduction of two-component jets (Racusin et al. 2008) or reverse shock contributions (Uhm & Beloborodov 2007; Genet et al. 2007), offer solutions but introduce additional complexities and parameters, making it challenging to fully interpret the variability observed in GRB behaviors (Panaitescu & Kumar 2001, 2002; Yost et al. 2003).

Despite its strengths, this model predictions conflict with our key findings. Late time central engine activity may lead to the production of some late time flares. In this case, one would expect that for GRBs with plateau, the average flare occurrence time may be later than for GRBs without late energy injection (i.e., without plateau). Alternatively, the average ratio of the flare width to its peak time, ( $w/t_{\text{pk}}$ ) is expected to be lower if the energy injection that leads to the flare occurs at later times, as the flares will have shorter time to develop and spread. Both these predictions are in contradiction to both our key findings. The fact that  $t_{\text{pk}}$  is the same for both sub-samples suggests it is not a delayed central engine activity that produces the flares. The constant ratio ( $w/t_{\text{pk}} \approx 1$ ) is a strong indication of a similar motion, such as internal expansion of shells that is proportional to the radius, and originated at early times (during, or close to the observed prompt phase).

An alternative idea for explaining the plateau is that of an observer located off the jet axis (viewing angle effect), initially suggested by Eichler & Granot (2006). As was shown by several authors (Toma et al. 2006; Eichler 2014), an observer that is located slightly off the jet axis will observe an X-ray plateau, provided that the jet is structured (e.g., has an angle-dependent Lorentz factor). As the jet decelerates, progressively brighter material closer to the core becomes visible, leading to the shallow flux evolution observed during the plateau phase (Beniamini & Nakar 2019; Beniamini et al. 2020a). This model successfully predicts the plateau duration and flux as functions of the jet structure and the observer's viewing angle, establishing correlations between these properties and the GRB's prompt emission characteristics (Beniamini et al. 2020a). However, while the model can account for achromatic plateaus in some bursts, it struggles to explain chromatic afterglows (Eichler & Granot 2006; Oganesyanyan et al. 2020).

This model was recently extended to explain X-ray flares as delayed, deboosted versions of gamma-ray pulses produced in the jet's core, while the plateau phase is interpreted as deboosted afterglow emission from the core (Beniamini et al. 2020b). In this scenario, energy dissipation that lead to flares would occur, on the average, at the same radius,  $R$  for different GRBs. Different observers will observe the flares at different times, since the observed time is given by  $t \sim R/\mathcal{D}^2c$ , where  $\mathcal{D}$  is the Doppler boost, which is angle-dependent. Therefore, it is expected that GRBs with plateaus would show flares occurring at later times. However, this expectation is contradicted by our finding in point (1), where the flare peak time,  $t_{\text{pk}}$ , is on average the same for GRBs with and without a plateau. Additionally, Duque et al. (2022) discuss that the off-axis interpretation can only account for a subset of observed flares, particularly those seen earlier, at  $\lesssim 1000$  seconds. However, as discussed in section 3.1, considering early flares did not affect the result in point (1). Moreover, the consistent patterns and similarity in flare characteristics, such as width, flare asymmetry, and variability relative to the continuum, suggest that viewing angles might not significantly influence the observed properties.

A third model that was recently suggested is that the plateau originates from emission that occurs during the coasting phase of the propagating forward shock (Shen & Matzner 2012; Dereli-Bégué et al. 2022). This phase precedes the self-similar decaying phase that produces the late time afterglow. As was shown by Dereli-Bégué et al. (2022), this model can naturally account for both the X-ray and optical signals without requiring complex modifications or additional parameters beyond the standard GRB "fireball" model framework. Its key difference than the classical GRB "fireball" evolution, is the assumption that during the coasting phase, the GRB Lorentz factor does not exceeds a few tens (rather than the common assumption of Lorentz factor of a few hundreds). Furthermore, this model requires that the explosion occurs into a low-density stellar wind environment, as is indeed expected for massive star GRB progenitors. This model effectively explains the plateau phase as due to synchrotron radiation from particles accelerated by the forward shock during the coasting phase.

This model provides several testable predictions. These include: (1) the expectation that bursts with long plateau phases should not exhibit high-energy (GeV) emission or strong thermal components;<sup>4</sup> (2) both chromatic and a-chromatic breaks are expected, resulting from the fact that different observed frequencies may be below or above the characteristic synchrotron cooling break (see Dereli-Bégué et al. 2022, for details).

The results found here are consistent with the predictions of this model. For GRBs with a lower Lorentz factor, energy dissipation processes producing the flares, such as, e.g., collisions, are expected to occur at smaller radii compared to GRBs with high-Lorentz factor. For example, internal collisions originating from internal variability of typical time  $\delta t$  are expected at radius  $r \sim \Gamma^2 c \delta t$ , where  $\Gamma$  is the jet Lorentz factor. However, since the observed time is  $t \sim r/\Gamma^2 c$ , the dependence on the unknown Lorentz factor cancels, and the observed flaring time is similar in both low- and high-Lorentz factor GRBs. Similar argument holds for the ratio of flare widths to peak time.

## 6. SUMMARY AND CONCLUSION

In this paper, we considered the X-ray light curves of 89 GRBs. We find that 61 (69%) of all GRBs have flares, and 57 (64%) have plateaus. However, no correlation was found between the existence of flares and existence of a plateau. We therefore conclude that the existence of flares is independent of the existence of an X-ray plateau.

We then analyzed the properties of flares that were detected in those 61 GRBs. Of those GRBs, 42 (68%) have a plateau, while 19 do not. We found no statistical difference between the flare peak times and the ratio of flare width to peak time,  $w/t_{pk} \sim 1$  between GRBs with and without plateau. From these results, presented in section 3.1, we conclude that the flare properties of GRBs are similar regardless of the presence or absence of plateau phases in the GRBs X-ray light curves.

We then confronted these results with three leading theories discussed in the literature as a possible origin of the plateau: (i) late time energy injection; (ii) observers located at different viewing angles; and (iii) emission during the coasting phase, which requires the terminal jet Lorentz factor to not exceed a few tens. We find that the former two models predictions are inconsistent with the observed results. In a late energy injection model, one expects that at least some of the flares will occur at later times, and may be narrower than without it, which is not seen. Similarly, for an observer located off the jet axis, the observed flare time should appear later than for an observer located on the line of sight, due to the different Doppler boosting. The predictions of the low Lorentz factor model, on the other hand, are consistent with the results presented here. For GRBs with low Lorentz factors, one expects the flares to originate at smaller radius relative to GRBs with larger Lorentz factor. But since the observed time depends on the Lorentz factor, an observer will see the flares at (average) similar times, regardless of the difference Lorentz factors. Our results therefore provide an independent support to the idea that the origin of the plateau phase is GRBs with lower Lorentz factor, of the order of few tens, as presented in Dereli-Bégué et al. (2022).

This study, employing the approach to fitting the underlying afterglow with physically motivated models and clearly defining the flare properties, can be expanded to a larger sample in X-rays and extended using data obtained at different wavelengths, such as UV and optical, to address the debate between X-ray flares and optical flashes. Notably, the recent *SVOM* and upcoming *ULTRASAT* space telescopes aim to increase the number of GRBs detected in these bands by providing rapid, arcsecond-level localization of bursts to trigger ground-based facilities. In addition, combining data from Swift and SVOM could allow for a better sampling of the light-curve, in particular between the time range  $10^3$  and  $10^4$ s.

If correct, this model has a strong potential to provide valuable clues about the underlying physics of GRB progenitors and jet dynamics. Coasting Lorentz factor of several tens that may be in a substantial fraction of GRBs could significantly release physical constraints on the jet acceleration, and progenitor properties. It is therefore of high importance to find independent measures that could validate or invalidate this idea. The results presented here suggest such a strong, independent support.

<sup>4</sup> GRBs classified as class II in Dereli-Bégué et al. (2022) have long and flat plateaus and do not show GeV emissions. Additionally, their variability time  $\Delta t_{\min}$  is expected to be  $> 5$ . For example, GRBs classified in class III may have a short and decaying plateau and might exhibit GeV emission.

1 We wish to thank Dr. Paz Beniamini and Miss. Gowri A. for enlightening discussions on the manuscript. This work  
 2 made use of data supplied by the UK Swift Science Data Centre at the University of Leicester. AP, acknowledges  
 3 support from the European Union via ERC consolidating grant #773062 (acronym O.M.J.) and from the Israel Space  
 4 Agency via grant number 6766. FR acknowledges support from the Swedish National Space Agency (2021-00180 and  
 5 2022-00205)

*Facilities:* Swift-XRT

*Software:* MultiNest

## REFERENCES

- Abdo, A. A., Ackermann, M., Ajello, M., et al. 2011, *ApJL*, 734, L27, doi: [10.1088/2041-8205/734/2/L27](https://doi.org/10.1088/2041-8205/734/2/L27)
- Barthelmy, S. D., Cannizzo, J. K., Gehrels, N., et al. 2005, *ApJL*, 635, L133, doi: [10.1086/499432](https://doi.org/10.1086/499432)
- Beniamini, P., Duque, R., Daigne, F., & Mochkovitch, R. 2020a, *MNRAS*, 492, 2847, doi: [10.1093/mnras/staa070](https://doi.org/10.1093/mnras/staa070)
- Beniamini, P., Granot, J., & Gill, R. 2020b, *MNRAS*, 493, 3521, doi: [10.1093/mnras/staa538](https://doi.org/10.1093/mnras/staa538)
- Beniamini, P., & Nakar, E. 2019, *MNRAS*, 482, 5430, doi: [10.1093/mnras/sty3110](https://doi.org/10.1093/mnras/sty3110)
- Bernardini, M. G., Margutti, R., Chincarini, G., Guidorzi, C., & Mao, J. 2011, *A&A*, 526, A27, doi: [10.1051/0004-6361/201015703](https://doi.org/10.1051/0004-6361/201015703)
- Burrows, D. N., Romano, P., Falcone, A., et al. 2005, *Science*, 309, 1833, doi: [10.1126/science.1116168](https://doi.org/10.1126/science.1116168)
- Chincarini, G., Moretti, A., Romano, P., et al. 2007, *ApJ*, 671, 1903, doi: [10.1086/521591](https://doi.org/10.1086/521591)
- Chincarini, G., Mao, J., Margutti, R., et al. 2010, *MNRAS*, 406, 2113, doi: [10.1111/j.1365-2966.2010.17037.x](https://doi.org/10.1111/j.1365-2966.2010.17037.x)
- Curran, P. A., Starling, R. L. C., O'Brien, P. T., et al. 2008, *A&A*, 487, 533, doi: [10.1051/0004-6361:200809652](https://doi.org/10.1051/0004-6361:200809652)
- Dereli-Bégué, H., Pe'er, A., Ryde, F., et al. 2022, *Nature Communications*, 13, 5611, doi: [10.1038/s41467-022-32881-1](https://doi.org/10.1038/s41467-022-32881-1)
- Duque, R., Beniamini, P., Daigne, F., & Mochkovitch, R. 2022, *MNRAS*, 513, 951, doi: [10.1093/mnras/stac938](https://doi.org/10.1093/mnras/stac938)
- Eichler, D. 2014, *ApJL*, 787, L32, doi: [10.1088/2041-8205/787/2/L32](https://doi.org/10.1088/2041-8205/787/2/L32)
- Eichler, D., & Granot, J. 2006, *ApJL*, 641, L5, doi: [10.1086/503667](https://doi.org/10.1086/503667)
- Evans, P. A., Beardmore, A. P., Page, K. L., et al. 2007, *A&A*, 469, 379, doi: [10.1051/0004-6361:20077530](https://doi.org/10.1051/0004-6361:20077530)
- . 2009, *MNRAS*, 397, 1177, doi: [10.1111/j.1365-2966.2009.14913.x](https://doi.org/10.1111/j.1365-2966.2009.14913.x)
- Falcone, A. D., Burrows, D. N., Lazzati, D., et al. 2006, *ApJ*, 641, 1010, doi: [10.1086/500655](https://doi.org/10.1086/500655)
- Falcone, A. D., Morris, D., Racusin, J., et al. 2007, *ApJ*, 671, 1921, doi: [10.1086/523296](https://doi.org/10.1086/523296)
- Fan, Y., & Piran, T. 2006, *MNRAS*, 369, 197, doi: [10.1111/j.1365-2966.2006.10280.x](https://doi.org/10.1111/j.1365-2966.2006.10280.x)
- Fan, Y. Z., & Wei, D. M. 2005, *MNRAS*, 364, L42, doi: [10.1111/j.1745-3933.2005.00102.x](https://doi.org/10.1111/j.1745-3933.2005.00102.x)
- Fenimore, E. E., Epstein, R. I., & Ho, C. 1993, *A&AS*, 97, 59
- Feroz, F., Hobson, M. P., & Bridges, M. 2009, *MNRAS*, 398, 1601, doi: [10.1111/j.1365-2966.2009.14548.x](https://doi.org/10.1111/j.1365-2966.2009.14548.x)
- Gehrels, N., Chincarini, G., Giommi, P., et al. 2004, *ApJ*, 611, 1005, doi: [10.1086/422091](https://doi.org/10.1086/422091)
- Genet, F., Daigne, F., & Mochkovitch, R. 2007, *MNRAS*, 381, 732, doi: [10.1111/j.1365-2966.2007.12243.x](https://doi.org/10.1111/j.1365-2966.2007.12243.x)
- Giannios, D. 2006, *A&A*, 455, L5, doi: [10.1051/0004-6361:20065578](https://doi.org/10.1051/0004-6361:20065578)
- Gibson, S. L., Wynn, G. A., Gompertz, B. P., & O'Brien, P. T. 2018, *MNRAS*, 478, 4323, doi: [10.1093/mnras/sty1363](https://doi.org/10.1093/mnras/sty1363)
- Granot, J., Königl, A., & Piran, T. 2006, *MNRAS*, 370, 1946, doi: [10.1111/j.1365-2966.2006.10621.x](https://doi.org/10.1111/j.1365-2966.2006.10621.x)
- Granot, J., & Kumar, P. 2006, *MNRAS*, 366, L13, doi: [10.1111/j.1745-3933.2005.00121.x](https://doi.org/10.1111/j.1745-3933.2005.00121.x)
- Granot, J., & Sari, R. 2002, *ApJ*, 568, 820, doi: [10.1086/338966](https://doi.org/10.1086/338966)
- Grupe, D., Gronwall, C., Wang, X.-Y., et al. 2007, *ApJ*, 662, 443, doi: [10.1086/517868](https://doi.org/10.1086/517868)
- Hinshaw, G., Weiland, J. L., Hill, R. S., et al. 2009, *ApJS*, 180, 225, doi: [10.1088/0067-0049/180/2/225](https://doi.org/10.1088/0067-0049/180/2/225)
- Ioka, K., Kobayashi, S., & Zhang, B. 2005, *ApJ*, 631, 429, doi: [10.1086/432567](https://doi.org/10.1086/432567)
- Krolik, J. H., & Pier, E. A. 1991, *ApJ*, 373, 277, doi: [10.1086/170048](https://doi.org/10.1086/170048)
- Kumar, P., & Zhang, B. 2015, *PhR*, 561, 1, doi: [10.1016/j.physrep.2014.09.008](https://doi.org/10.1016/j.physrep.2014.09.008)

- Lazzati, D., Blackwell, C. H., Morsony, B. J., & Begelman, M. C. 2011, *MNRAS*, 411, L16, doi: [10.1111/j.1745-3933.2010.00984.x](https://doi.org/10.1111/j.1745-3933.2010.00984.x)
- Lazzati, D., & Perna, R. 2007, *MNRAS*, 375, L46, doi: [10.1111/j.1745-3933.2006.00273.x](https://doi.org/10.1111/j.1745-3933.2006.00273.x)
- Margutti, R., Bernardini, G., Barniol Duran, R., et al. 2011, *MNRAS*, 410, 1064, doi: [10.1111/j.1365-2966.2010.17504.x](https://doi.org/10.1111/j.1365-2966.2010.17504.x)
- Mészáros, P. 2006, *Reports on Progress in Physics*, 69, 2259, doi: [10.1088/0034-4885/69/8/R01](https://doi.org/10.1088/0034-4885/69/8/R01)
- Meszáros, P., & Rees, M. J. 1993, *ApJ*, 405, 278, doi: [10.1086/172360](https://doi.org/10.1086/172360)
- . 1997, *ApJ*, 476, 232, doi: [10.1086/303625](https://doi.org/10.1086/303625)
- Mészáros, P., Rees, M. J., & Wijers, R. A. M. J. 1998, *ApJ*, 499, 301, doi: [10.1086/305635](https://doi.org/10.1086/305635)
- Metzger, B. D., Giannios, D., Thompson, T. A., Bucciantini, N., & Quataert, E. 2011, *MNRAS*, 413, 2031, doi: [10.1111/j.1365-2966.2011.18280.x](https://doi.org/10.1111/j.1365-2966.2011.18280.x)
- Norris, J. P., Bonnell, J. T., Kazanas, D., et al. 2005, *ApJ*, 627, 324, doi: [10.1086/430294](https://doi.org/10.1086/430294)
- Nousek, J. A., Kouveliotou, C., Grupe, D., et al. 2006, *ApJ*, 642, 389, doi: [10.1086/500724](https://doi.org/10.1086/500724)
- O’Brien, P. T., Willingale, R., Osborne, J., et al. 2006, *ApJ*, 647, 1213, doi: [10.1086/505457](https://doi.org/10.1086/505457)
- Oganesyan, G., Ascenzi, S., Branchesi, M., et al. 2020, *ApJ*, 893, 88, doi: [10.3847/1538-4357/ab8221](https://doi.org/10.3847/1538-4357/ab8221)
- Panaitescu, A., & Kumar, P. 2001, *ApJL*, 560, L49, doi: [10.1086/324061](https://doi.org/10.1086/324061)
- . 2002, *ApJ*, 571, 779, doi: [10.1086/340094](https://doi.org/10.1086/340094)
- Perri, M., Guetta, D., Antonelli, L. A., et al. 2007, *A&A*, 471, 83, doi: [10.1051/0004-6361:20066227](https://doi.org/10.1051/0004-6361:20066227)
- Piran, T. 2004, *Reviews of Modern Physics*, 76, 1143, doi: [10.1103/RevModPhys.76.1143](https://doi.org/10.1103/RevModPhys.76.1143)
- Racusin, J. L., Karpov, S. V., Sokolowski, M., et al. 2008, *Nature*, 455, 183, doi: [10.1038/nature07270](https://doi.org/10.1038/nature07270)
- Racusin, J. L., Oates, S. R., Schady, P., et al. 2011, *ApJ*, 738, 138, doi: [10.1088/0004-637X/738/2/138](https://doi.org/10.1088/0004-637X/738/2/138)
- Rees, M. J., & Meszaros, P. 1992, *MNRAS*, 258, 41P, doi: [10.1093/mnras/258.1.41P](https://doi.org/10.1093/mnras/258.1.41P)
- Ronchini, S., Oganesyan, G., Branchesi, M., et al. 2021, *Nature Communications*, 12, 4040, doi: [10.1038/s41467-021-24246-x](https://doi.org/10.1038/s41467-021-24246-x)
- Sari, R., Piran, T., & Narayan, R. 1998, *ApJL*, 497, L17+, doi: [10.1086/311269](https://doi.org/10.1086/311269)
- Shen, R., & Matzner, C. D. 2012, *ApJ*, 744, 36, doi: [10.1088/0004-637X/744/1/36](https://doi.org/10.1088/0004-637X/744/1/36)
- Srinivasaragavan, G. P., Dainotti, M. G., Fraija, N., et al. 2020, *ApJ*, 903, 18, doi: [10.3847/1538-4357/abb702](https://doi.org/10.3847/1538-4357/abb702)
- Tagliaferri, G., Goad, M., Chincarini, G., et al. 2005, *Nature*, 436, 985, doi: [10.1038/nature03934](https://doi.org/10.1038/nature03934)
- Toma, K., Ioka, K., Yamazaki, R., & Nakamura, T. 2006, *ApJL*, 640, L139, doi: [10.1086/503384](https://doi.org/10.1086/503384)
- Uhm, Z. L., & Beloborodov, A. M. 2007, *ApJL*, 665, L93, doi: [10.1086/519837](https://doi.org/10.1086/519837)
- Willingale, R., O’Brien, P. T., Osborne, J. P., et al. 2007, *ApJ*, 662, 1093, doi: [10.1086/517989](https://doi.org/10.1086/517989)
- Yi, S.-X., Du, M., & Liu, T. 2022, *ApJ*, 924, 69, doi: [10.3847/1538-4357/ac35e7](https://doi.org/10.3847/1538-4357/ac35e7)
- Yi, S.-X., Xi, S.-Q., Yu, H., et al. 2016, *ApJS*, 224, 20, doi: [10.3847/0067-0049/224/2/20](https://doi.org/10.3847/0067-0049/224/2/20)
- Yost, S. A., Harrison, F. A., Sari, R., & Frail, D. A. 2003, *ApJ*, 597, 459, doi: [10.1086/378288](https://doi.org/10.1086/378288)
- Zhang, B., Fan, Y. Z., Dyks, J., et al. 2006, *ApJ*, 642, 354, doi: [10.1086/500723](https://doi.org/10.1086/500723)

## APPENDIX

## A. MODELS USED FOR FITTING THE DATA

In our analysis, we consider the following models for fitting the underlying afterglow emission. First, we consider two classes of models, referring to the medium into which the blast-wave expands: (i) a "wind" model, in which the ambient density drops with radius as  $n(r) \propto r^{-2}$ , and the "interstellar medium (ISM)" model, which assumes a constant ambient density profile,  $n(r) \propto r^0$ . These two different assumptions affect the evolution of the blast wave Lorentz factor, and are therefore considered separately. We further assume that electrons are accelerated to a power-law in the propagating blast wave, with a power law index  $p$ . The observed signal is due to synchrotron emission from these electrons. The spectral and temporal slopes depend on the observed frequency, relative to the characteristic synchrotron frequencies: the peak frequency,  $\nu_m$  and the cooling frequency,  $\nu_c$ . E.g., different slopes are expected for  $\{\nu_m, \nu_c\} < \nu^{\text{obs.}}$ ,  $\nu_m < \nu^{\text{obs.}} < \nu_c$ , etc. We refer to the nomenclature defined in [Dereli-Bégué et al. \(2022\)](#) to label the different models. Since we are focusing on data in the X-ray band obtained by the *Swift*-XRT instrument, our analysis considers the scenarios labeled as C/F and E in [Dereli-Bégué et al. \(2022\)](#), for which the time evolution of the spectrum is given by:

$$\text{Case C/F :} \quad \{\nu_m, \nu_c\} < \nu^{\text{obs.}} \quad F_\nu \propto \begin{cases} t_{\text{obs.}}^{(2-p)/2} \nu^{-p/2} & t_{\text{obs.}} < T_a \\ t_{\text{obs.}}^{(2-3p)/4} \nu^{-p/2} & t_{\text{obs.}} > T_a \end{cases} \quad (\text{A1})$$

$$\text{Case E :} \quad \nu_m < \nu^{\text{obs.}} < \nu_c \quad F_\nu \propto \begin{cases} t_{\text{obs.}}^{(1-p)/2} \nu^{-(p-1)/2} & t_{\text{obs.}} < T_a \\ t_{\text{obs.}}^{(1-3p)/4} \nu^{-(p-1)/2} & t_{\text{obs.}} > T_a \end{cases} \quad (\text{A2})$$

Here,  $t_{\text{obs.}}$  is the observed time and  $T_a$  is the end of the plateau time. According to our interpretation, this time marks the transition between the coasting and the decelerating phase of the expansion. In this transition, the index of the electron injection function  $p$  is assumed to be constant, thereby linking the temporal slope before the plateau to that after the plateau, enforcing rigidity in our models.

For the ISM model, we refer to the two segments labeled as G and H in [Sari et al. \(1998\)](#):

$$\text{Case G :} \quad \nu_m < \nu^{\text{obs.}} < \nu_c \quad F_\nu \propto t_{\text{obs.}}^{(3-3p)/4} \nu^{-(p-1)/2} \quad (\text{A3})$$

$$\text{Case H :} \quad \{\nu_m, \nu_c\} < \nu^{\text{obs.}} \quad F_\nu \propto t_{\text{obs.}}^{(2-3p)/4} \nu^{-p/2} \quad (\text{A4})$$

In this case, we assume that the transition between coasting phase and self-similar phase happens before the first *Swift*-XRT observations or during the steep decay. Consequently, in our analysis, we do not consider the coasting phase for ISM models.

The Cases C/F and E for the wind environment and the cases H and G for the ISM environment, represent different spectral regimes depending on the cooling state of the plasma behind the shock, namely on the position of the cooling frequency  $\nu_c$  with respect to the injection frequency  $\nu_m$ . Finally, on top of each of emission model, we further consider the possibility of observing (i) a steep decay, assumed in this analysis to be associated to the end of the prompt phase, (ii) a jet break and (iii) zero, one or two flares. This led us to fit a total of 36 models to each observed afterglow light curve. 12 models are considered for the "wind" environment scenario, differ by existence/in-existence of jet break, number of flares (0,1,2) and spectral regime (C/F or E). 24 models are considered for the "ISM" case, which, in addition to the above, consider existence or in-existence of a steep decay (in the "wind" model, which is used to fit GRBs with plateau, a steep decay always assumed to exist). The models are summarized in [Table A0](#).

All afterglow components at the exception of the flares are assumed to be power-law functions of time, namely the flux in the X-ray band is  $F_x(t) \propto t^a$ . The power-law index  $a$  is motivated by the considered component and the physical scenario as described in the equations above, at the exception of the index of the fast decay which is constrained to be greater than 2. All components making an empirical afterglow model form a continuous function in time. The analysis is performed in log space, meaning that the variable becomes  $T \equiv \log(t)$  and the observable is  $\mathfrak{F} \equiv \log(F)$ . For instance, a model of afterglow in the wind environment with a steep decay, a jet break and such that  $\{\nu_m, \nu_c\} \ll \nu^{\text{obs.}}$ ,

is expressed as

$$\mathfrak{F} = \begin{cases} \alpha T + A & T < T_1 \\ \beta T + A + (\alpha - \beta)T_1 & T_1 < T < T_2 \\ \zeta T + A + (\alpha - \beta)T_1 + (\beta - \zeta)T_2 & T_2 < T < T_3 \\ (\zeta + q)T + A + (\alpha - \beta)T_1 + (\beta - \zeta)T_2 + (\zeta - \eta)T_3 & T_3 > T \end{cases} \quad (\text{A5})$$

Here,  $A$  represents the normalization of the flux,  $T_1$  is the transition time between the steep decay and the first afterglow segment, namely the plateau,  $T_2 \equiv T_a$  is the time at which the blast-wave transitions from the plateau to a steeper decay (interpreted as coasting to the decelerating phase), and  $T_3$  is the time of the jet break. For this specific regime, the parameters  $\beta$  and  $\zeta$  are not independent: they both depend on the power-law index  $p$  of the injected electrons at the shock front. We use this constraint, by setting  $\beta$  and  $\zeta$  to the parameter dependencies presented in Equations A1, A2, A3, A4, and consider  $p$  to be the free model parameter. For the example of Equation A5, we have  $\beta = (2 - p)/2$  and  $\zeta = (2 - 3p)/4$ . In addition, after the jet break, the afterglow slope is steeper than  $\zeta$  and rather than fitting directly for the slope, we fit for the difference  $q$  between the post-jet-break slope and  $\zeta$ , such that the new slope is  $\zeta + q$ . We allow for the extra degree of freedom in the choice of the value of  $q$ , as the jet break is not sharp, but rather is observed over a long duration, in particular for observers that are off the jet axis. These techniques add some rigidity to the models and allow for a straightforward interpretation of the results. An example of the fitting results are presented in Figure A1 in Appendix A.1.

**Table A0.** Comparison of models for different theoretical scenarios. For wind scenarios (Cases C/F and E), the models include conditions for steep decay, jet break, and number of flares. All models incorporate the early steep decay phase, with optional jet break and flare presence. For ISM scenarios (Cases H and G), the models include similar conditions with additional differentiation, where the early steep decay is also optional. The table details the presence of steep decay, jet break, and number of flares for each model.

Environment	Model Name	Steep Decay	Jet Break	Number of Flares
Wind	<b>Case C/F and E</b>			
	C1 / E1	Yes	No	0
	C2 / E2	Yes	Yes	0
	C3 / E3	Yes	No	1
	C4 / E4	Yes	No	2
	C5 / E5	Yes	Yes	1
	C6 / E6	Yes	Yes	2
ISM	<b>Case H and G</b>			
	H1 / G1	No	No	0
	H2 / G2	No	No	1
	H3 / G3	No	No	2
	H4 / G4	Yes	No	0
	H5 / G5	Yes	No	1
	H6 / G6	Yes	No	2
	H7 / G7	No	Yes	0
	H8 / G8	No	Yes	1
	H9 / G9	No	Yes	2
	H10 / G10	Yes	Yes	0
	H11 / G11	Yes	Yes	1
H12 / G12	Yes	Yes	2	

#### A.1. Example fit to the X-ray Light curve of GRB 190719C

To visualize the fitting process, in Figure A1 (left-top), we illustrate the X-ray count light-curve of GRB 190719C obtained by the *Swift*-XRT instrument. The data is fitted in log scale, therefore, for consistency we present the data in log-scale as well. The data are superposed with the fit results (blue) from a selected best model where three-segments



BPL model, i.e. with two break times, and two Norris functions are used to fit two flares. It represents the case C/F in the wind where steep decay, plateau phase and the late afterglow decay are present, but no jet break. This model is shown as C4 in Table A0. In Figure A1 (left-bottom), we present the residuals between the best model and the data which shows how well the model describes the data. The corner plot of the posterior probability distributions of the fit parameters and the covariances between the fit parameters is displayed in Figure A1 (right).

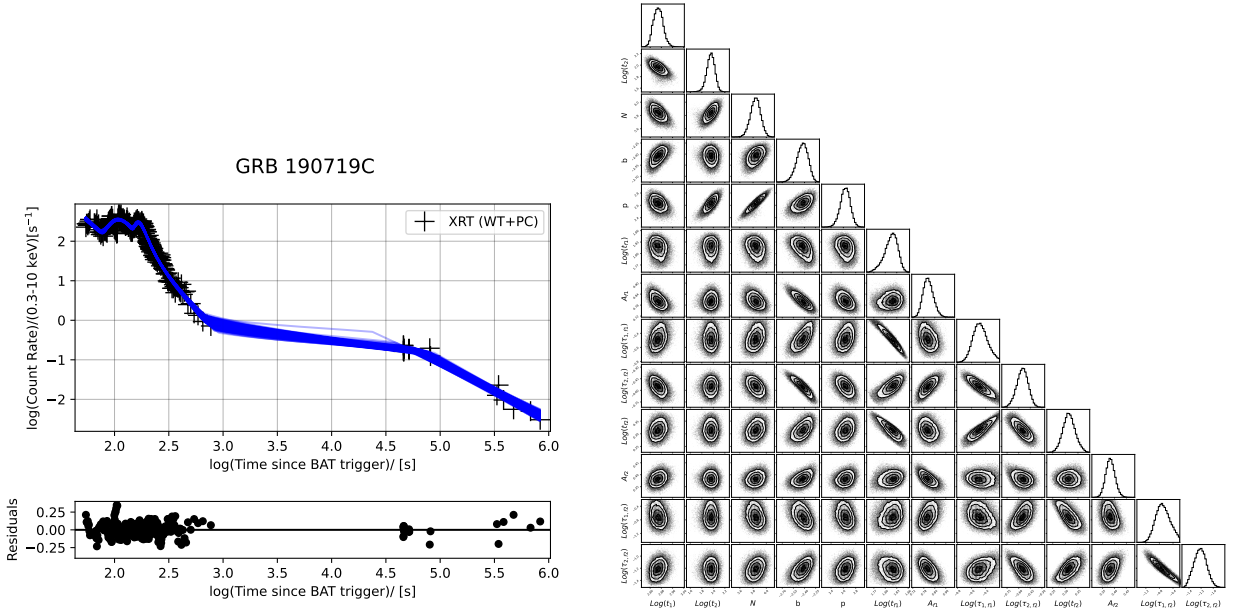


**Figure A1.** Left-top: The X-ray LC of GRB 190719C. The black crosses represent the XRT-WTSLEW, XRT-WT, XRT-PC mode data. The errors correspond to a significance of one sigma. The blue lines represent the posterior distributions of the best fit model. Left-bottom: The residuals between the best model and the data. Right: The corner plot of the posterior probability distributions of the fit parameters and the covariances between the fit parameters.

## B. BURSTS EXCLUDED FROM THE SAMPLE

Out of the 100 GRBs in our sample, we exclude 11 GRBs listed in Table B0. The exclusion criteria was misidentification of flares, which compromised the underlying afterglow emission and failures of the different afterglow models to adequately fit the data. When this happened, identified flares extend more than the data, most of the time up to  $> 10^5$  s which corresponds to the more than the half of the dynamical range. As a result, the allowed variability in the flare shape replaces the underlying afterglow, which is at nearly all time dominated by flare emission. Therefore, such a exclusion was done to avoid misinterpretation of the model parameters.

**Table B0.** The list of excluded 11 GRBs from the main sample. Column 1: GRB name, Column 2: The flare width, Column 3: The flare isotropic energy.

GRB name	$w$ (s)	$E_{\text{iso},f}$ (ergs)
221009A	$0.4 \times 10^5$	$10^{51}$
210610A	$0.7 \times 10^7$	$10^{52}$
210104A	$0.5 \times 10^7$	$10^{51}$
201221A	$0.3 \times 10^5$	$10^{52}$
190114C	$0.3 \times 10^7$	$10^{51}$
170728B	$0.3 \times 10^7$	$10^{52}$
161129A	$0.8 \times 10^7$	$10^{51}$
160117B	$0.4 \times 10^8$	$10^{51}$
150910A	$0.2 \times 10^7$	$10^{52}$
150403A	$0.1 \times 10^8$	$10^{53}$
140614A	$0.8 \times 10^8$	$10^{52}$

### C. SAMPLE OF 61 GRBS WITH FLARES AND DERIVED PARAMETERS

In our analysis, the fit parameters are computed using the maximum posterior estimate (MAP) method. The derived parameters and their errors are calculated using the marginalized posterior distributions (MPD). As discussed in section 2.4, the selection of the best fit models is based on the AIC, and AICc criteria. The results show that the AICc condition is consistently satisfied by the data. Additionally, in most cases, the AIC condition is also met with the same model. Therefore, we only present the AICc in Table C1, along with the derived parameters obtained from the best fit parameters. The parameter errors are computed by using the credible intervals (e.g., 68% for  $1\sigma$ ) derived directly from the posterior samples of the fit parameters.

**Table C1.** Derived parameters for selected GRBs with flares (Part 1). Column 1: GRB name, Column 2: Best model, Columns 3: corrected Akaike Information Criterion of the best model, Columns 4-9: Derived parameters with their errors—flare peak time, flare width, flare asymmetry, total flare isotropic energy in units of  $10^{50}$  erg, flare width to the flare peak time ratio, and flare peak flux-to-underlying continuum ratio. When the best model has two flares, the entry corresponding to this GRB is on two rows.

GRB	Best	AICc	$t_{\text{pk}}$	$w$	$k$	$E_{\text{iso},f}$	$w/t_{\text{pk}}$	$\Delta F_{\text{flare}}/F_{\text{cont.}}$
name	model		(s)	(s)		( $10^{50}$ erg)		
220117A	C4	251	$189^{+1.6}_{-2.04}$	$434^{+240}_{-157}$	$0.37^{+0.03}_{-0.03}$	$360^{+22.6}_{-25.5}$	$2.3^{+1.3}_{-0.8}$	$9.7^{+4.2}_{-2.6}$
			$1124^{+67}_{-68}$	$5203^{+1054}_{-1499}$	$0.45^{+0.01}_{-0.01}$	$373^{+55.1}_{-68.2}$	$4.6^{+0.8}_{-1.2}$	$6.9^{+2.5}_{-1.9}$
220101A	C5	801	$167^{+6.7}_{-7.8}$	$298^{+68}_{-75}$	$0.50^{+0.02}_{-0.02}$	$5769^{+785}_{-115}$	$1.8^{+0.3}_{-0.4}$	$11.2^{+4.4}_{-3.6}$
211024B	C4	442	$6621^{+169}_{-186}$	$1.4 \times 10^{4+2 \times 10^4}_{-0.6 \times 10^4}$	$0.38^{+0.05}_{-0.05}$	$123^{+15.4}_{-31.1}$	$2.1^{+3.0}_{-1.0}$	$178^{+52}_{-77}$
			$1.4 \times 10^{4+145}_{-153}$	$1.1 \times 10^{5+1.6 \times 10^4}_{-2.6 \times 10^4}$	$0.32^{+0.01}_{-0.01}$	$103^{+3.5}_{-3.5}$	$7.9^{+1.2}_{-1.9}$	$36.5^{+13.5}_{-10.5}$
210905A	G3	272	$98^{+1.1}_{-1.2}$	$155^{+91}_{-69}$	$0.37^{+0.04}_{-0.03}$	$239^{+18.6}_{-21.5}$	$1.6^{+0.9}_{-0.7}$	$2.3^{+0.3}_{-0.2}$
			$371^{+1.4}_{-1.2}$	$140^{+17.9}_{-16.1}$	$0.75^{+0.01}_{-0.02}$	$1208^{+101}_{-91}$	$0.4^{+0.05}_{-0.04}$	$17.4^{+1.0}_{-0.9}$
210722A	G9	278	$124^{+0.8}_{-0.8}$	$1210^{+54}_{-102}$	$0.30^{+0.004}_{-0.004}$	$11.9^{+0.5}_{-0.5}$	$9.7^{+0.4}_{-0.8}$	$2.3^{+0.1}_{-0.1}$
			$8545^{+439}_{-468}$	$3.8 \times 10^{4+1 \times 10^4}_{-1.2 \times 10^4}$	$0.45^{+0.02}_{-0.01}$	$11.7^{+1.1}_{-1.2}$	$4.4^{+1.0}_{-1.3}$	$3.3^{+0.5}_{-0.4}$
210702A	H8	523	$5245^{+308}_{-435}$	$1 \times 10^{4+1.3 \times 10^4}_{-0.6 \times 10^4}$	$0.47^{+0.09}_{-0.05}$	$37.9^{+13.3}_{-10.9}$	$2.0^{+2.4}_{-1.1}$	$1.0^{+0.2}_{-0.2}$
210610B	C5	651	$102^{+1.7}_{-1.9}$	$80^{+2.7}_{-2.4}$	$0.57^{+0.02}_{-0.02}$	$46.9^{+1.3}_{-0.9}$	$0.8^{+0.03}_{-0.02}$	$37.6^{+5.3}_{-3.9}$
210504A	E3	104	$460^{+6.9}_{-7.0}$	$210^{+601}_{-134}$	$0.41^{+0.12}_{-0.10}$	$11.8^{+1.9}_{-2.9}$	$0.5^{+1.3}_{-0.3}$	$4.6^{+0.8}_{-0.7}$
210420B	E3	121	$716^{+42.9}_{-33.6}$	$438^{+362}_{-180}$	$0.64^{+0.09}_{-0.12}$	$5.1^{+1.6}_{-1.4}$	$0.6^{+0.5}_{-0.2}$	$2.8^{+0.4}_{-0.3}$
210411C	G9	70	$174^{+3.9}_{-4.7}$	$101^{+308}_{-37.7}$	$0.48^{+0.16}_{-0.12}$	$32.9^{+12.1}_{-8.1}$	$0.6^{+1.7}_{-0.2}$	$4.9^{+0.7}_{-0.6}$
			$663^{+113}_{-92}$	$1573^{+1650}_{-865}$	$0.47^{+0.06}_{-0.04}$	$30.5^{+11.6}_{-10.8}$	$2.4^{+2.1}_{-1.2}$	$0.9^{+0.2}_{-0.2}$
201104B	C3	112	$202^{+3.2}_{-3.6}$	$303^{+913}_{-242}$	$0.30^{+0.12}_{-0.06}$	$3.1^{+0.65}_{-0.68}$	$1.5^{+4.5}_{-1.2}$	$0.7^{+0.1}_{-0.1}$
200205B	C6	523	$455^{+1.9}_{-1.7}$	$1774^{+348}_{-221}$	$0.31^{+0.01}_{-0.01}$	$168^{+2.3}_{-2.2}$	$3.9^{+0.8}_{-0.5}$	$17.8^{+1.0}_{-0.9}$
			$534^{+2.9}_{-2.9}$	$183^{+27.5}_{-25.8}$	$0.74^{+0.01}_{-0.01}$	$47.5^{+2.1}_{-2.4}$	$0.3^{+0.05}_{-0.05}$	$2.3^{+0.2}_{-0.2}$
191221B	C5	954	$169^{+1.9}_{-2.0}$	$1382^{+140}_{-244}$	$0.33^{+0.01}_{-0.004}$	$28.9^{+1.0}_{-0.9}$	$8.2^{+0.8}_{-1.4}$	$2.5^{+0.1}_{-0.1}$
190829A	C5	789	$1524^{+29.4}_{-26.6}$	$1460^{+280}_{-154}$	$0.54^{+0.03}_{-0.03}$	$28.9^{+1.0}_{-0.9}$	$1.0^{+0.2}_{-0.1}$	$3.0^{+0.1}_{-0.1}$
190719C	C4	685	$175^{+1.1}_{-1.1}$	$202^{+286}_{-96}$	$0.35^{+0.06}_{-0.06}$	$589^{+20}_{-25}$	$1.2^{+1.6}_{-0.5}$	$1.4^{+0.1}_{-0.1}$
			$133^{+3.2}_{-3.0}$	$266^{+167}_{-80}$	$0.43^{+0.03}_{-0.04}$	$154^{+9.4}_{-9.5}$	$2.0^{+1.3}_{-0.6}$	$5.4^{+0.4}_{-0.4}$
190114A	E6	130	$232^{+6.5}_{-10.1}$	$39.8^{+37.2}_{-9.1}$	$0.55^{+0.09}_{-0.11}$	$67^{+26}_{-22}$	$0.2^{+0.2}_{-0.04}$	$3.0^{+1.6}_{-0.9}$
			$1688^{+700}_{-219}$	$4800^{+6242}_{-4158}$	$0.45^{+0.10}_{-0.06}$	$34.2^{+61}_{-25}$	$2.5^{+2.4}_{-2.1}$	$0.9^{+0.8}_{-0.2}$
190106A	C6	290	$100^{+0.5}_{-0.5}$	$790^{+350}_{-368}$	$0.22^{+0.02}_{-0.01}$	$36.6^{+2.5}_{-2.5}$	$7.9^{+3.5}_{-3.7}$	$1.3^{+0.1}_{-0.1}$
			$258^{+38.9}_{-12.1}$	$141^{+289}_{-96}$	$0.56^{+0.15}_{-0.20}$	$1.5^{+1.7}_{-0.61}$	$0.5^{+0.9}_{-0.3}$	$0.7^{+0.2}_{-0.1}$
181110A	C6	588	$168^{+1.2}_{-1.2}$	$1434^{+121}_{-183}$	$0.32^{+0.01}_{-0.004}$	$798^{+16.4}_{-16.7}$	$8.5^{+0.7}_{-1.1}$	$7.2^{+0.9}_{-0.8}$
			$118^{+2.1}_{-2.1}$	$984^{+36.1}_{-67}$	$0.34^{+0.01}_{-0.004}$	$536^{+17.9}_{-18.3}$	$8.3^{+0.3}_{-0.6}$	$6.9^{+0.6}_{-0.5}$
181020A	G12	1669	$242^{+0.6}_{-0.6}$	$2331^{+64}_{-123}$	$0.31^{+0.002}_{-0.002}$	$942^{+10.3}_{-10.4}$	$9.6^{+0.3}_{-0.5}$	$6.2^{+0.1}_{-0.1}$
			$375^{+0.7}_{-0.8}$	$2623^{+1565}_{-1311}$	$0.21^{+0.02}_{-0.01}$	$103^{+4.7}_{-4.5}$	$7.0^{+4.2}_{-3.5}$	$1.1^{+0.04}_{-0.04}$
181010A	C5	208	$140^{+13.2}_{-27.0}$	$94^{+242}_{-50}$	$0.53^{+0.18}_{-0.16}$	$1.3^{+1.0}_{-0.6}$	$0.8^{+1.5}_{-0.4}$	$1.1^{+0.7}_{-0.2}$
180728A	E4	978	$2411^{+38.1}_{-37.3}$	$2927^{+2965}_{-1228}$	$0.43^{+0.06}_{-0.05}$	$0.26^{+0.46}_{-0.07}$	$1.2^{+1.2}_{-0.5}$	$1.4^{+0.1}_{-0.1}$
			$5226^{+2268}_{-1252}$	$2784^{+18002}_{-1935}$	$0.44^{+0.18}_{-0.12}$	$0.3^{+1.7}_{-0.2}$	$0.5^{+3.0}_{-0.3}$	$1.9^{+18.4}_{-1.2}$
180720B	C4	3434	$110^{+1.8}_{-1.7}$	$69^{+17.4}_{-12.5}$	$0.71^{+0.04}_{-0.04}$	$32.2^{+3.4}_{-3.2}$	$0.6^{+0.2}_{-0.1}$	$1.2^{+0.1}_{-0.1}$
			$362^{+5.8}_{-5.4}$	$2675^{+177}_{-315}$	$0.36^{+0.01}_{-0.004}$	$53.7^{+2.5}_{-2.5}$	$7.4^{+0.5}_{-0.8}$	$1.4^{+0.1}_{-0.1}$
180624A	E4	1487	$192^{+1.0}_{-0.7}$	$87^{+10.6}_{-6.7}$	$0.66^{+0.02}_{-0.02}$	$309^{+12.1}_{-9.1}$	$0.5^{+0.1}_{-0.04}$	$26.9^{+1.9}_{-1.3}$
			$444^{+5.6}_{-7.0}$	$403^{+60}_{-65}$	$0.63^{+0.01}_{-0.02}$	$524^{+16.5}_{-22.2}$	$0.9^{+0.1}_{-0.1}$	$53^{+4.2}_{-5.3}$
180620B	E6	367	$165^{+5.4}_{-4.9}$	$918^{+206}_{-280}$	$0.40^{+0.02}_{-0.01}$	$61.9^{+2.9}_{-3.1}$	$5.6^{+1.2}_{-1.7}$	$3.9^{+0.6}_{-0.5}$
			$5956^{+807}_{-841}$	$1.1 \times 10^{4+1.4 \times 10^4}_{-0.5 \times 10^4}$	$0.49^{+0.09}_{-0.04}$	$8.2^{+4.1}_{-2.8}$	$1.9^{+2.3}_{-0.8}$	$1.1^{+0.2}_{-0.2}$
180329B	E6	440	$166^{+1.1}_{-1.1}$	$150^{+38.8}_{-25.8}$	$0.43^{+0.02}_{-0.02}$	$161^{+4.5}_{-7.1}$	$0.9^{+0.2}_{-0.2}$	$94^{+6.2}_{-6.9}$
			$234^{+2.3}_{-2.0}$	$202^{+58}_{-41.2}$	$0.39^{+0.02}_{-0.03}$	$44^{+4.5}_{-3.7}$	$0.9^{+0.2}_{-0.2}$	$2.3^{+0.5}_{-0.3}$
180325A	C3	381	$81^{+0.8}_{-1.8}$	$15.1^{+3.0}_{-1.1}$	$0.56^{+0.06}_{-0.05}$	$93.8^{+9.5}_{-8.1}$	$0.2^{+0.03}_{-0.01}$	$14.0^{+1.2}_{-1.0}$
180205A	G8	89	$181^{+1.8}_{-1.8}$	$86^{+161}_{-43.7}$	$0.42^{+0.07}_{-0.08}$	$4.8^{+0.7}_{-10.6}$	$0.5^{+0.9}_{-0.2}$	$4.5^{+1.0}_{-0.7}$
171222A	C3	212	$337^{+19.0}_{-17.1}$	$558^{+131}_{-94}$	$0.51^{+0.02}_{-0.03}$	$225^{+20.3}_{-20.0}$	$1.6^{+0.3}_{-0.2}$	$4.5^{+0.8}_{-0.8}$
170714A	C4	3227	$5285^{+211}_{-258}$	$2.8 \times 10^{4+1 \times 10^4}_{-1.1 \times 10^4}$	$0.38^{+0.02}_{-0.01}$	$120^{+9.8}_{-9.2}$	$5.3^{+1.7}_{-2.1}$	$4.8^{+0.2}_{-0.2}$
			$1.3 \times 10^{4+82}_{-86}$	$1.2 \times 10^{5+0.8 \times 10^4}_{-1.5 \times 10^4}$	$0.32^{+0.01}_{-0.004}$	$81.8^{+2.2}_{-2.2}$	$8.8^{+0.6}_{-1.1}$	$7.6^{+0.6}_{-0.5}$
170705A	C5	992	$217^{+0.7}_{-0.7}$	$1800^{+19.0}_{-39.4}$	$0.35^{+0.001}_{-0.001}$	$245^{+2.1}_{-2.1}$	$8.3^{+0.1}_{-0.2}$	$76^{+2.9}_{-2.9}$



Table C1 (Continued)

GRB	Best	AICc	$t_{pk}$	$w$	$k$	$E_{iso,f}$	$w/t_{pk}$	$\Delta F_{flare}/F_{cont.}$
name	model		(s)	(s)		( $10^{50}$ erg)		
170607A	E4	576	$152^{+8.6}_{-7.3}$	$162^{+24.2}_{-12.7}$	$0.58^{+0.03}_{-0.03}$	$3.6^{+0.2}_{-0.2}$	$1.1^{+0.1}_{-0.1}$	$1.8^{+0.2}_{-0.1}$
			$9050^{+685}_{-708}$	$3.5 \times 10^4^{+1.5 \times 10^4}_{-1.5 \times 10^4}$	$0.45^{+0.03}_{-0.02}$	$1.9^{+0.4}_{-0.5}$	$3.8^{+1.5}_{-1.5}$	$0.9^{+0.1}_{-0.1}$
170604A	3H	535	$130^{+2.4}_{-2.2}$	$42.0^{+2.8}_{-3.0}$	$0.73^{+0.01}_{-0.02}$	$37.3^{+3.3}_{-3.1}$	$0.3^{+0.02}_{-0.03}$	$9.5^{+0.9}_{-0.8}$
			$364^{+1.0}_{-1.1}$	$2623^{+1037}_{-1192}$	$0.28^{+0.02}_{-0.01}$	$84^{+1.9}_{-1.8}$	$7.2^{+2.8}_{-3.3}$	$12.1^{+0.4}_{-0.4}$
170531B	G3	397	$168^{+0.4}_{-0.4}$	$255^{+40.1}_{-39.7}$	$0.38^{+0.01}_{-0.01}$	$52^{+1.7}_{-2.3}$	$126^{+1.3}_{-1.4}$	$48.2^{+1.8}_{-2.5}$
			$576^{+0.6}_{-0.6}$	$711^{+294}_{-187}$	$0.33^{+0.02}_{-0.02}$	$98^{+5.2}_{-4.3}$	$76^{+1.1}_{-1.1}$	$62^{+2.0}_{-2.8}$
170519A	E4	820	$203^{+0.4}_{-0.4}$	$67^{+2.9}_{-2.8}$	$0.72^{+0.01}_{-0.01}$	$28.4^{+0.5}_{-0.5}$	$0.3^{+0.01}_{-0.01}$	$49.7^{+1.7}_{-1.7}$
			$2153^{+1824}_{-883}$	$2099^{+2432}_{-1028}$	$0.64^{+0.12}_{-0.16}$	$2.1^{+2.0}_{-1.0}$	$0.9^{+0.5}_{-0.3}$	$2.6^{+5.5}_{-1.2}$
170405A	H9	420	$162^{+0.7}_{-0.7}$	$131^{+95}_{-44.8}$	$0.36^{+0.03}_{-0.04}$	$242^{+10.3}_{-11.7}$	$0.8^{+0.6}_{-0.3}$	$2.7^{+0.1}_{-0.1}$
			$6555^{+1139}_{-1245}$	$1.6 \times 10^4^{+1.7 \times 10^4}_{-1.0 \times 10^3}$	$0.48^{+0.08}_{-0.03}$	$242^{+10.3}_{-11.7}$	$2.5^{+2.2}_{-1.4}$	$2.0^{+0.8}_{-0.4}$
170202A	C3	108	$100^{+4.1}_{-3.2}$	$41.0^{+41.1}_{-15.1}$	$0.65^{+0.09}_{-0.15}$	$18.5^{+6.3}_{-4.5}$	$0.4^{+0.4}_{-0.1}$	$0.6^{+0.1}_{-0.04}$
170113A	C4	273	$93^{+0.4}_{-0.5}$	$21.1^{+14.3}_{-8.3}$	$0.44^{+0.06}_{-0.05}$	$78.4^{+1.6}_{-1.5}$	$0.2^{+0.2}_{-0.1}$	$1.8^{+0.3}_{-0.2}$
170113A	C4	273	$94^{+0.8}_{-0.9}$	$581^{+163}_{-143}$	$0.34^{+0.01}_{-0.01}$	$25.8^{+4.6}_{-5.8}$	$6.2^{+1.7}_{-1.5}$	$10.3^{+1.4}_{-1.3}$
161219B	C6	737	$2480^{+82}_{-79}$	$14036^{+1626}_{-2806}$	$0.42^{+0.01}_{-0.01}$	$0.11^{+0.01}_{-0.01}$	$5.7^{+0.6}_{-1.1}$	$4.8^{+0.7}_{-0.6}$
			$406^{+4.2}_{-4.3}$	$315^{+55}_{-45.4}$	$0.67^{+0.03}_{-0.03}$	$0.4^{+0.03}_{-0.03}$	$0.8^{+0.1}_{-0.1}$	$38.6^{+2.9}_{-2.6}$
161117A	G12	560	$124^{+0.6}_{-0.6}$	$168^{+30.2}_{-23.9}$	$0.45^{+0.01}_{-0.01}$	$364^{+7.9}_{-8.9}$	$1.4^{+0.2}_{-0.2}$	$42.4^{+1.6}_{-1.5}$
			$7844^{+480}_{-512}$	$2.7 \times 10^4^{+1.3 \times 10^4}_{-1.2 \times 10^4}$	$0.46^{+0.03}_{-0.02}$	$27.8^{+4.4}_{-6.3}$	$3.5^{+1.6}_{-1.5}$	$1.8^{+0.2}_{-0.2}$
161108A	G6	416	$148^{+2.8}_{-2.8}$	$307^{+82}_{-72}$	$0.46^{+0.02}_{-0.02}$	$37.5^{+2.1}_{-3.3}$	$2.1^{+0.5}_{-0.5}$	$3.6^{+0.3}_{-0.3}$
			$1398^{+1175}_{-557}$	$420^{+3034}_{-315}$	$0.37^{+0.13}_{-0.11}$	$3.6^{+23.6}_{-3.2}$	$0.3^{+1.9}_{-0.2}$	$32.3^{+294}_{-29.3}$
161017A	C6	1562	$409^{+1.2}_{-1.2}$	$4630^{+295}_{-557}$	$0.24^{+0.004}_{-0.003}$	$337^{+6.8}_{-6.7}$	$11.3^{+0.7}_{-1.4}$	$1.7^{+0.1}_{-0.1}$
			$201^{+1.4}_{-1.4}$	$1712^{+35.1}_{-64}$	$0.34^{+0.003}_{-0.003}$	$88^{+2.8}_{-2.8}$	$8.5^{+0.2}_{-0.3}$	$3.2^{+0.1}_{-0.1}$
160804A	G12	1464	$433^{+2.2}_{-2.2}$	$4194^{+87}_{-153}$	$0.31^{+0.004}_{-0.003}$	$11^{+0.4}_{-0.4}$	$9.7^{+0.2}_{-0.4}$	$1.5^{+0.1}_{-0.1}$
			$1.5 \times 10^4^{+2 \times 10^3}_{-2 \times 10^3}$	$2.3 \times 10^4^{+3.8 \times 10^4}_{-1.0 \times 10^4}$	$0.49^{+0.11}_{-0.06}$	$0.7^{+0.4}_{-0.2}$	$1.5^{+2.3}_{-0.6}$	$0.7^{+0.2}_{-0.1}$
160425A	G5	1004	$300^{+0.6}_{-0.6}$	$287^{+37.5}_{-30.9}$	$0.40^{+0.01}_{-0.01}$	$34.1^{+0.4}_{-0.4}$	$1.0^{+0.1}_{-0.1}$	$115^{+6.3}_{-5.4}$
160410AS	E3	77	$192^{+32.4}_{-39.3}$	$600^{+479}_{-416}$	$0.45^{+0.07}_{-0.04}$	$7.1^{+3.0}_{-2.3}$	$3.0^{+2.1}_{-1.9}$	$1.1^{+1.4}_{-0.4}$
160228A	H8	95	$181^{+2.8}_{-3.3}$	$75^{+568}_{-61}$	$0.39^{+0.13}_{-0.13}$	$0.6^{+2.5}_{-2.1}$	$0.4^{+1.5}_{-0.3}$	$1.0^{+0.5}_{-0.3}$
160227A	E4	859	$215^{+0.8}_{-0.8}$	$83^{+6.7}_{-6.3}$	$0.68^{+0.01}_{-0.01}$	$186^{+4.9}_{-5.2}$	$0.4^{+0.03}_{-0.03}$	$16.4^{+0.7}_{-0.7}$
			$422^{+1.1}_{-1.0}$	$345^{+16.8}_{-16.0}$	$0.80^{+0.003}_{-0.004}$	$137^{+3.1}_{-3.0}$	$0.8^{+0.03}_{-0.03}$	$9.9^{+0.7}_{-0.6}$
160131A	E4	582	$197^{+8.0}_{-11.3}$	$871^{+204}_{-268}$	$0.46^{+0.02}_{-0.01}$	$24^{+3.2}_{-4.5}$	$4.4^{+0.9}_{-1.2}$	$1.9^{+0.6}_{-0.5}$
			$6948^{+296}_{-297}$	$29744^{+17935}_{-15924}$	$0.39^{+0.05}_{-0.03}$	$6.2^{+1.0}_{-1.1}$	$4.3^{+2.5}_{-2.2}$	$0.6^{+0.1}_{-0.04}$
151027B	C3	66	$3626^{+944}_{-2708}$	$3263^{+14307}_{-2535}$	$0.47^{+0.23}_{-0.13}$	$35.7^{+121}_{-13.1}$	$1.2^{+3.1}_{-0.5}$	$2.3^{+40.7}_{-0.9}$
151027A	C6	909	$132^{+0.4}_{-0.4}$	$1180^{+121}_{-196}$	$0.30^{+0.01}_{-0.003}$	$49^{+0.82}_{-0.81}$	$9.0^{+0.9}_{-1.5}$	$35.8^{+1.9}_{-1.9}$
			$307^{+1.9}_{-1.8}$	$3038^{+205}_{-380}$	$0.28^{+0.01}_{-0.004}$	$4.9^{+0.2}_{-0.2}$	$9.9^{+0.7}_{-1.2}$	$1.7^{+0.1}_{-0.1}$
151021A	C4	294	$232^{+22.8}_{-11.8}$	$185^{+323}_{-77}$	$0.46^{+0.09}_{-0.10}$	$352^{+12}_{-13}$	$0.8^{+1.4}_{-0.3}$	$1.1^{+0.2}_{-0.1}$
			$129^{+1.0}_{-1.2}$	$1046^{+167}_{-242}$	$0.31^{+0.01}_{-0.01}$	$20.5^{+6.5}_{-5.1}$	$8.1^{+1.3}_{-1.9}$	$4.3^{+0.3}_{-0.4}$
150821A	G6	670	$714^{+8.4}_{-7.6}$	$633^{+154}_{-87}$	$0.50^{+0.02}_{-0.03}$	$7.0^{+0.73}_{-0.67}$	$0.9^{+0.2}_{-0.1}$	$1.7^{+0.05}_{-0.04}$
			$1126^{+5.5}_{-5.6}$	$264^{+341}_{-148}$	$0.36^{+0.08}_{-0.07}$	$0.53^{+0.1}_{-0.1}$	$0.2^{+0.3}_{-0.1}$	$0.7^{+0.1}_{-0.1}$
150818A	E3	301	$79^{+0.3}_{-0.3}$	$421^{+435}_{-291}$	$0.19^{+0.04}_{-0.02}$	$1.03^{+0.1}_{-0.1}$	$5.3^{+5.5}_{-3.7}$	$3.1^{+0.3}_{-0.3}$
150727A	E3	473	$825^{+52}_{-62}$	$4008^{+704}_{-1111}$	$0.45^{+0.01}_{-0.01}$	$0.2^{+0.02}_{-0.02}$	$4.9^{+0.7}_{-1.2}$	$1.2^{+0.1}_{-0.1}$
150314A	G11	704	$1.1 \times 10^4^{+4.3 \times 10^3}_{-1.5 \times 10^3}$	$6.4 \times 10^4^{+4 \times 10^6}_{-3.5 \times 10^4}$	$0.77^{+0.08}_{-0.06}$	$98^{+25.1}_{-16.2}$	$5.8^{+257}_{-3.0}$	$1.5^{+0.2}_{-0.2}$
150206A	H3	813	$1911^{+92}_{-167}$	$11386^{+5574}_{-5633}$	$0.32^{+0.03}_{-0.02}$	$1722^{+539}_{-199}$	$6.1^{+2.7}_{-2.9}$	$8.1^{+2.5}_{-0.7}$
			$2362^{+4.5}_{-4.4}$	$2.0 \times 10^4^{+8.6 \times 10^3}_{-8.8 \times 10^3}$	$0.21^{+0.02}_{-0.01}$	$431^{+35.6}_{-31.8}$	$8.3^{+3.6}_{-3.7}$	$1.6^{+0.2}_{-0.2}$
141221A	H3	69	$358^{+33.7}_{-28.4}$	$590^{+748}_{-231}$	$0.50^{+0.06}_{-0.05}$	$14.1^{+3.4}_{-2.3}$	$1.6^{+1.9}_{-0.5}$	$4.4^{+1.1}_{-0.9}$
			$345^{+8.0}_{-7.8}$	$431^{+1394}_{-356}$	$0.33^{+0.16}_{-0.08}$	$4.1^{+1.5}_{-1.5}$	$1.1^{+3.9}_{-0.9}$	$1.6^{+0.6}_{-0.4}$
141121A	C4	882	$606^{+31.1}_{-25.2}$	$244^{+338}_{-146}$	$0.70^{+0.07}_{-0.13}$	$23.7^{+9.2}_{-10.7}$	$0.4^{+0.5}_{-0.2}$	$2.8^{+0.6}_{-0.4}$
			$6671^{+207}_{-267}$	$2.6 \times 10^4^{+1.6 \times 10^4}_{-1.4 \times 10^4}$	$0.40^{+0.05}_{-0.02}$	$42.2^{+3.6}_{-6.4}$	$3.9^{+2.4}_{-2.1}$	$13.8^{+3.8}_{-2.5}$
140907A	C3	111	$206^{+26.5}_{-18.7}$	$601^{+766}_{-437}$	$0.38^{+0.08}_{-0.05}$	$2.6^{+1.1}_{-1.0}$	$2.8^{+3.4}_{-2.0}$	$3.9^{+2.1}_{-1.2}$
140710A	G2	47	$365^{+12.4}_{-15.3}$	$140^{+131}_{-35.1}$	$0.60^{+0.12}_{-0.16}$	$0.3^{+0.7}_{-0.5}$	$0.4^{+0.3}_{-0.1}$	$10.4^{+2.3}_{-1.9}$
140703A	C5	176	$120^{+1.6}_{-1.7}$	$13.0^{+21.5}_{-3.0}$	$0.52^{+0.08}_{-0.11}$	$58^{+24}_{-14}$	$0.1^{+0.2}_{-0.03}$	$0.8^{+0.1}_{-0.1}$
140629A	C5	119	$202^{+38.7}_{-51}$	$229^{+380}_{-102}$	$0.52^{+0.09}_{-0.07}$	$8.5^{+9.0}_{-3.1}$	$1.1^{+1.5}_{-0.3}$	$1.5^{+0.9}_{-0.4}$